Wideband Coaxial Cable Transfer Impedance for Karoo Array Telescope

by

Joely Andrianina Andriambeloson

Thesis presented in partial fulfilment of the requirements for
the degree of Master of Science in Engineering at
the University of Stellenbosch

Department of Electronic and Electrical Engineering,
University of Stellenbosch

Supervisor: Prof. Howard Charles Reader

December 2011

Declaration

By submitting this thesis electronically, I declare that the entirety of the work contained therein is my own, original work, that I am the sole author thereof (save to the extent explicitly otherwise stated), that reproduction and publication thereof by Stellenbosch University will not infringe any third party rights and that I have not previously in its entirety or in part submitted it for obtaining any qualification.

Date: December 2011

Abstract

Through the Karoo Array Telescope, and its extension MeerKAT, South Africa is demonstrating its capabilities to host the most powerful radio telescope ever, the Square Kilometre Array (SKA). This new interferometer is intended to assist radio astronomers in unlocking the mysteries concealed in the far regions of the universe. A thorough investigation of Radio Frequency Interference (RFI) sources at each stage of the design becomes relevant for the success of the project.

The electromagnetic coupling through coaxial cables is the main focus of this thesis since 90% of the Electromagnetic Compatibility (EMC) problems come from inadequate system layout and grounding, where cabling plays the major role. Interest revolves around better noise immunity, low radiation and cost. Transfer impedance (Z_T) and shielding effectiveness (SE) are used as the cable selection criteria. Several measurements of coaxial cables identified on KAT-7 have been performed for Z_T characterisation from 300 kHz up to 1.3 GHz. A current injection method is used to identify the Z_T for the low frequency region. We derived the high frequency part of Z_T, with a reverberation chamber technique (RC) measuring shielding effectiveness. At first, we calibrated the RC according to the relevant IEC 61000-4-21 standard and evaluated the result with an Open Area Test Site (OATS) E-field estimation. The accuracy of the E-field within the chamber is also addressed, based on statistical analysis of the chamber's independent samples.

The OATS E-field equivalent determination showed a good correlation with the OATS E-field data of a standard radiator. A coaxial air-line Z_T verified the theoretical Z_T model within 7 dB and showed the expected 20 dB/decade slope variation. Furthermore, the braiding porpoising effect has been noticed with some cable samples. Here, a variation less than 20 dB/decade occurs at lower frequency. Then, the slope changes to 20 dB/decade at high frequency. This study illustrates a practical comparison of cable performance and constitutes a first approach to RFI mitigation of the MeerKAT cabling system.

Opsomming

Deur middel van die Karoo Reeks Teleskoop, asook sy uitbreiding MeerKAT, demonstreer Suid-Afrika sy vermo om die mees kragtige radioteleskoop ooit, die Vierkante Kilometer Reeks (SKA), te vestig. Hierdie nuwe interferometer is bedoel om radiosterrekundiges te help in die ontsluiting van die geheimenisse wat versteek is in die verre reike van die heelal. 'n Deeglike ondersoek van Radio Frekwensie Steurings (RFS) bronne by elke stadium van die ontwerp is belangrik vir die sukses van die projek.

Die elektromagnetiese koppeling deur koaksiale kabels is die hooffokus van hierdie tesis, aangesien 90% van die elektromagnetiese versoenbaarheid (EMV) probleme ontstaan as gevolg van onvoldoende stelsel-uitleg en beaarding, waar kabels die hoofrol speel. Beter ruis-immuniteit, lae straling en koste vorm die areas van belang. Oordragimpedansie (Z_T) en afskermingsdoeltreffendheid (SE) word gebruik as die kabelkeuringskriteria. Verskeie metings van koaksiale kabels wat op KAT-7 gedentifiseer is, is uitgevoer vir Z_T karakterisering van 300 kHz tot 1,3 GHz. 'n Stroom-induseringsmetode is gebruik om die Z_T vir die lae-frekwensiebereik te identifiseer. Ons het die ho-frekwensie deel van Z_T afgelei met 'n weerkaatsingskamer tegniek (RC) wat afskermingsdoeltreffendheid meet. Eerstens het ons die RC gekalibreer volgens die relevante IEC 61000-4-21 standaard en die resultaat met 'n Ope Area Toetsterrein (OAT) E-veld benadering gevalueer. Die akkuraatheid van die E-veld in die kamer is ook aangespreek, gebaseer op 'n statistiese analise van die kamer se onafhanklike monsters.

Die OAT E-veld ekwivalente benadering het goed met die OAT E-veld data van 'n standaard uistraler gekorreleer. 'n Koaksiale lugmedium-transmissielyn Z_T bevestig die teoretiese Z_T model binne 7 dB en het ook die verwagte 20 dB/dekade variasie in helling getoon. Verder is die golwende effek oor die kabelomvlegting opgemerk met sekere kabels. Hier is 'n variasie van minder as 20 dB/dekade gevind by die laer frekwensie. Dan verander die helling na 20 dB/dekade teen ho frekwensie. Hierdie studie toon 'n praktiese vergelyking van die verrigting van die kabel en 'n eerste benadering tot RFS tempering van die MeerKAT kabelstelsel.

Acknowledgements

In the first place, my utmost gratitude and sincere praise to our Lord Jesus Christ for his limitless blessings. “But by the grace of God I am what I am”, I Cor15:10.

I gratefully acknowledge Prof. Howard Reader for giving me the opportunity to do a Masters degree in EMC and allowing me to join the EMRIN group. Thanks for your supervision and guidance throughout the development of this thesis. Your feedback concerning my writing and crucial advice helped me a lot improving my knowledge and experience not only in EMC but also in engineering science.

Many thanks go in particular to Dr Gideon Wiid for his time, help and contributions during all the phases of this work. It started from the very early stage of the research until the writing of the thesis. Thanks for reading my manuscript and most importantly the translation.

Very special thanks to my family for all the encouragement and enduring support during all my studies.

I would like also to express my gratitude to the following people:

- The South African SKA project and the National Research Foundation for the funding over the years I have been here in Stellenbosch
- Wessel Croukamp, Wynand Van Eeden and Lincol Saunders for the coaxial air-line and the maintenance of the reverberation chamber.
- Robert Anderson and Martin Siebers for their technical expertise during all the measurements I performed at the RF laboratory.
- Danie Janse Van Rensburg and Johan Strydom for giving the opportunity to use their standard radiator for my experiment.
- The EMRIN group and all the students in the room 212 for their assistance in a direct or indirect way. Thanks for the coffee and the pleasant environment.

Contents

List of Figures

List of Tables

Nomenclature

Symbols and Units

α_e	Electric Polarizability	m^3
α_m	Magnetic Polarizability	m^3
δ	Skin depth	m
ϵ	Electric Permittivity	F/m
μ	Magnetic Permeability	H/m
ω	Angular Frequency	rad/s
σ	Conductivity	S
f	Frequency	Hz
I_{CM}	Common Mode Current	A
M_{12}	Mutual Inductance	H/m
M_b	Porpoising Inductance	H/m
N_{Ind}	Number of Independent Samples	
N_S	Number of Samples	
R_{dc}	Resistance	Ω
$S(D/\lambda)$	Summing function	dB
V_{DM}	Differential Mode Voltage	V
Z_T	Transfer Impedance	Ω/m
ACF	Antenna Calibration Factor	
CCF	Chamber Calibration Factor	
CLF	Chamber Loading Factor	

IL	Insertion Loss
LUF	Lowest Usable Frequency
SE	Shielding Effectiveness

Abbreviations

CM	Common Mode
CP	Current Probe
CUT	Cable Under Test
DC	Direct Current
DM	Differential Mode
DUT	Device Under Test
EM	Electromagnetic
EMC	Electromagnetic Compatibility
EMI	Electromagnetic Interference
EMS	Electromagnetic Susceptibility
ERS	Emissions Reference Source
EUT	Equipment Under Test
GSM	Global System for Mobile
HF	High Frequency
IEC	International Electrotechnical Commission
KAT	Karoo Array Telescope
LF	Low Frequency
LPDA	Log Periodic Dipole Arrays
NPL	National Physical Laboratory
OATS	Open Area Test Site
RC	Reverberation Chamber
RF	Radio Frequency
RFI	Radio Frequency Interference
SA	Spectrum Analyser
SKA	Square Kilometre Array
TE	Transverse Electric
TM	Transverse Magnetic
VNA	Vector Network Analyser

CHAPTER 1

Introduction

From the early stages of human knowledge until the present technological era, the clear night sky with its various bright wonders has fascinated people and influenced cultures and civilisations all around the world. Ancient civilisations, such as the Mayans, the Greeks, the Egyptians and others, have understood the essence of astronomy in everyday life. To be successful in agriculture for instance, they used the regular patterns of the sun and the moon to keep track of time and seasons. Many vestiges and ruins of these ancient times testify to the importance of astronomy to these developed societies.

Today, the progress of the radio astronomy science and technology, after the experiment of Karl Guthe Jansky, has dramatically improved our understanding of the universe. Aware of the undiscovered knowledge hidden in the far region of the sky, such as the mystery of dark energy, the existence of Earth-like planets or the topic concerning extra-terrestrial life, astronomers want to push forward the radio astronomy technology by building a mega radio telescope about hundred times more sensitive than today's biggest radio telescope [1]. This project is known as the Square Kilometre Array (SKA). The Republic of South Africa and Australia are the remaining countries bidding to host this challenging project.

1.1 The South African SKA Demonstrator Project

Through the Karoo Array Telescopes (KAT) and its extension MeerKAT, South Africa is demonstrating its technology capabilities in hosting the project. The MeerKAT interferometer is expected to be the most powerful radio telescope of the southern hemisphere, allowing a highly sensitive continuum survey level to μJy with 64 dishes of Gregorian offset configuration, until the SKA interferometer completion in 2024 [2]. The project is taking place in the Karoo region of the Northern Cape province, in a zone referred to as the central astronomy advantage area [1]. Currently, seven telescopes (KAT-7) have been completed as shown in figure 1.1.

Figure 1.1: The KAT-7 Dishes in 2010 [1]

1.2 Radio Astronomy and RFI

The Jansky (Jy) is not a familiar unit for engineers. For radio astronomers, it represents the amount of radio frequency (RF) energy per unit time per unit area per unit bandwidth. We have $1\,Jy = 10^{-26}\frac{W}{m^2 Hz}$. A question that comes to mind for an engineer is the sensitivity of MeerKAT if we are using the SI unit of power (Watt).

Andrew Clegg, from the U.S. National Science Foundation, calculated the equivalence in dBm of 1 Jy using the following assumption [3]. He considered a Global System for Mobile (GSM) transmitter antenna radiating a signal at 1.8 GHz ($\lambda = 0.17$ m) with a bandwidth of 200 kHz. He found that 1 $Jy = -204$ dBm and 1 $\mu Jy = -264$ dBm. This simple example shows us how sensitive the radio astronomy observations are likely to be.

This high sensitivity of the MeerKAT and the SKA interferometers requires a careful and thorough engineering examination of each stage of the design in order to lower the noise of the system. We must prevent self-made interference that would prevent our ability to receive the weakest signal from above. The risk of generating interference is high even if

the noise frequency is not precisely the same as the frequency of the observation. A big radio frequency interference (RFI) interest arises then for understanding sources which could interfere with the SKA spectrum.

According to Ellingson in [4], man-made sources are the potential limitation of the SKA-enabled science. The same author classified these sources into two categories as being from either internal, self-generated by the system, or external, from intentional and unintentional radio emissions. The MeerKAT site has already been proclaimed by the government as a radio quite zone, far from mobile and radio broadcasting systems. This reduces the external intentional RFI sources, but unintentional emissions from natural sources such as lightning, or the radiation caused by the power-line which goes into the site, are still potential candidates.

1.3 Motivation, Objectives and Methodology

Often, coaxial cables are directly exposed to the radiation from the environment. The external noise creates a common mode (CM) current on the cable braid and generates an internal voltage which superimposes on the transmitted signal. This corrupts the data and reduces the protection of equipment connected to the cable. Moreover, the importance of the volume occupied by the cabling system on electronic equipment is also another fact which increases the probability of electromagnetic interference (EMI) on the system.

Therefore, in this thesis, we are particularly interested in coaxial cable shielding examination. This investigation uses the concept of transfer impedance (Z_T) and shielding effectiveness (SE) to identify the performance of a cable under test (CUT) in terms of RFI. The Z_T of each CUT is determined from 300 kHz to 1.3 GHz using two methods: the reverberation chamber technique and the field to wire method of Benson et al. [5]. Basically, these experiments reproduce the environmental condition of the cable by subjecting it to a known signal level. However, prior to the Z_T investigation, the reverberation chamber is characterised according to the guidelines of the international standard for reverberation chambers (the IEC 61000-4-21).

1.4 Contents Overview

For a general understanding of the shielding principles, chapter 2 will present to the reader the concept and mathematical foundation of Z_T and SE. Published literature will

be reviewed for analytical models identification which govern the electromagnetic (EM) coupling on coaxial cables.

In chapter 3, we will focus plainly on the reverberation chamber technique. It begins with analytical characterisation of reverberation chambers, based on waveguide and cavity theory, and followed by a discussion concerning the IEC standard 61000-4-21 calibration procedure.

The results and discussion, relating the applications of the principles in the previous chapters, are presented in chapter 4 and chapter 5. Chapter 4 deals with the characterisation of our reverberation chamber, i.e. the chamber calibration and validation. Chapter 5 presents the wideband Z_T investigation.

Finally, in the last chapter, conclusions and recommendations concerning the thesis are given.

CHAPTER 2

Fundamentals of Coaxial Cable Shielding Analysis

Coaxial cables are found in most electronic systems for communication between modules. Often, a significant amount of space is occupied by the cabling. The interconnections between building blocks may lead to a galvanic loop formation. The larger the loop, the larger the potential coupling between systems. So, from an electromagnetic compatibility (EMC) point of view, coaxial cables constitute a source of electromagnetic interference (EMI), or electromagnetic susceptibility (EMS).

Before any experimental discussion on cable shielding evaluation, the theoretical developments of shielding effectiveness and transfer impedance are examined to enhance our background on shielded cable. This also introduces the reader to the terminology and the key concepts which will be used and investigated in later chapters.

2.1 Brief Description of Coaxial Cable

A coaxial cable is a transmission line which consists of two cylindrical conductors and a dielectric material sharing the same geometrical axis (figure 2.1). The outer conductor, also called shield, may be made of various materials. According to the construction of the shield, we can classify coaxial cables in two categories: a rigid or semi-rigid cable (figure 2.1.a) and a flexible cable (figure 2.1.a and figure 2.1.c). The rigid and the semi-rigid

cables are usually made of solid screen (a pipe). They are used particularly for a permanent setup. However, a flexible cable, which is constructed of braided wires, is suitable for variable setups.

2.2 Role of the Shield

The outer conductor acts as a current return path for the signal. According to Clayton Paul wires experiment [6, 7], the shield is used equally to reduce the capacitive coupling between the centre conductor and the external region.

2.3 EM Noise Coupling on Coaxial Cables

2.3.1 EM Noise Sources

Coaxial cables are sometimes placed in a hostile environment with electromagnetic (EM) noise present. The noise may originate from natural sources such as the sun activity, lightning strike, ionosphere activity; or from man-made sources like an EM impulse, radio broadcasting system or cellphone transmitter [8, 9]. The cable acts as an antenna and picks up the near-field and far-field energy via radiative coupling. A nearby item of noisy equipment connected to the system can also be considered as a source of noise from a conductive coupling path. In this case, the noise-current appears over the shield of the cable from the contact between the device and the cable [9]. A power line network is an example of conducted noise [10].

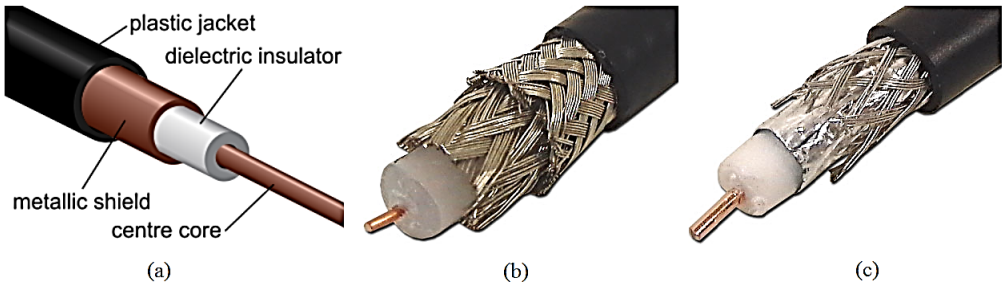

Figure 2.1: Example of coaxial cables: (a) Semi-rigid coaxial cable, (b) Double-braided coaxial cable, (c) Foiled and braided coaxial cable

Figure 2.2: Opening area located on the surface of a braided shield

2.3.2 Shielded Cable Imperfections

Due to the skin effect and the thickness of the outer conductor, the coaxial cable's shield is imperfect, even for homogeneous and solid tube such as the shield of a semi-rigid cable. Theoretically, a thick metallic sheath provides more shielding over a broadband frequency range, especially at low frequency. But, the need for flexibility in some applications introduces the use of thin shields and an overlapping braid of wires in coaxial cable manufacturing. On one hand, this procedure reduces the shielding effectiveness of the cable at lower frequency. On the other hand, the braid lowers the optical coverage of the cable due to the presence of holes over the metallic sheath (see figure 2.2).

2.3.3 Origin of Interference

When the coaxial cable is then illuminated by an external EM fields, these fields penetrate the imperfections of the shield and produce a radio frequency interference (RFI) in three ways [7, 11, 12]:

- By diffusion of electric and magnetic fields through the shield. This happens especially at low frequency, when the skin depth of the braid is bigger than its thickness. The current flowing over the external surface of the braid reaches the inner surface and couples capacitively or magnetically to the centre conductor.
- By magnetic and capacitive coupling through the apertures of the braid.
- By magnetic coupling between the overlapping strand. This situation occurs at the crossover (figure 2.2) at higher frequency, when the current follows over each individual wire in a helix-like direction [12]. The inner conductor couples to the outer conductor and this transmits the noise inside the cable.

More concerning the noise penetration through the shield will be discussed in section 2.5.

2.4 Importance of Cable Shielding Evaluation

Coaxial cables are essential for signal transport between instruments within a system. Interference might enter inside the cable from the imperfections of the shield. But the major question to be considered is whether the cable is making any difference to the immunity of the system or not.

For Tim Williams [13], the response is clear, 90 % of the EMC problems come from inadequate layout and grounding, where the cabling system plays a major role.

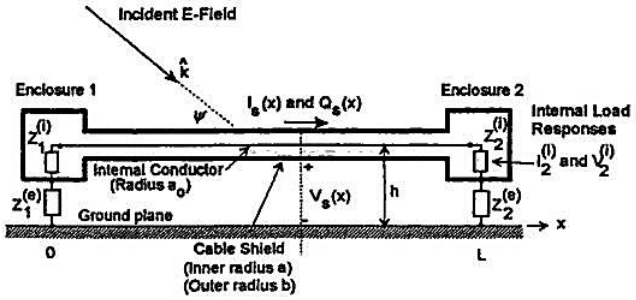

Figure 2.3: Model of a shielded coaxial line connecting two devices placed above a ground plane according to Tesche et al. [7]

According to Tesche et al. [7], a basic coaxial cable configuration connecting two pieces of equipment of input impedances Z_1^i and Z_2^i, above a ground plane, can be modelled as in figure 2.3. The cable's shield is always connected to the enclosure of each device, sometimes grounded to reduce the effect of capacitive coupling on the cable, and sometimes not. Both grounded and open-circuited setups are represented by the external impedances Z_1^e and Z_2^e. For this configuration, the cable and the two devices are exposed to the incident fields of the environment. The overall configuration shapes the RFI nature of the system. However, RFI mitigation from equipment is always possible by shielding effectiveness improvement. A simple diversion of current with proper grounding, or protecting the devices inside a screening enclosure, are two ways to achieve this goal.

Concerning the coaxial cables, the EM fields where they are placed cannot be easily predicted especially for a complex system such as MeerKAT. Moreover, a closed loop paths are always created by Z_1^e, Z_2^e and the outer conductor of the cable (figure 2.3). The system becomes most sensitive to magnetic fields from the crosstalk effect [6]. This leads to the creation of common mode (CM) current over the metallic sheath, which is stronger for a grounded configuration ($Z_1^e = Z_2^e = 0$). We remark also here, if we compare figure 2.3 and figure 2.4, that the cable arrangement and the distance L between the ground connections play an important role in the minimisation of the size of the loop. By reducing the size

of the loop, we decrease the noise impressed on the outer conductor but, the coupling through the shield is inevitable.

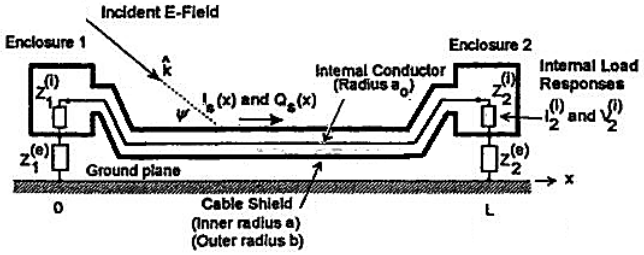

Figure 2.4: Modification of the cable layout to reduce the surface of the loop created by Z_1^e, Z_2^e and the shield of the coaxial cable. (After the model proposed by Tesche et al. [7])

Therefore, the evaluation and the selection of coaxial cables' shielding are crucial for RFI mitigation on the system.

2.5 Theoretical Evaluation of Cable shielding

We can evaluate the transmission of energy through the shield of a coaxial cable using two parameters:

- shielding effectiveness
- transfer impedance

2.5.1 Shielding effectiveness

2.5.1.1 Definition

From shielding theory [14, 15], the shielding effectiveness (SE) is defined, in terms of E or H-field, as the ratio of the incident and transmitted fields at M before and after positioning the shield (see figure 2.5). In this definition, the incident wave is assumed to be uniform and illuminating an infinite homogeneous shield.

According to Christopoulos [14], these two definitions of SE do not always produce a convergent results. Also, the E-field and H-field measurements are not convenient from practical point of view. As a consequence, the SE is sometimes evaluated in terms of voltage, current or power [16].

2.5.1.2 Shielding Mechanism

Let us consider an infinite conductor, of thickness d, dividing the space in two regions (the shielded area and the external environment), and a plane wave propagating from the left to the right-hand side of figure 2.5 representing the noise.

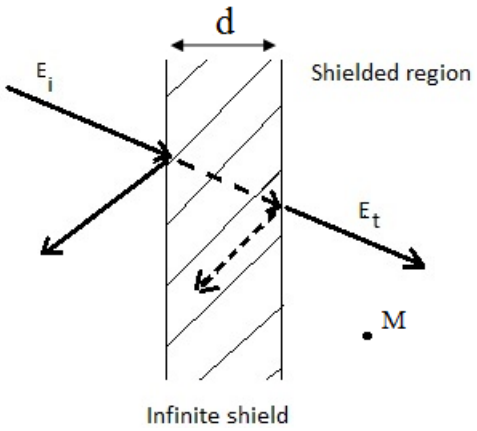

Figure 2.5: Plane wave approach of shielding process

At the first interface (air-shield), some part of the signal reflects back and some part penetrates into the conductor. The transmitted wave continues further. At the same time, it is attenuated by the shield. For low frequency signals, the conductor is electrically small. Thus, an amount of the energy reaches the shielded region. The rest reflects back into the conductor again which will go through multiple reflections from the two boundaries. This will make a further contribution to the signal transmitted in the protected region. Therefore, the effectiveness of the shield depends on [9, 14]:

- the reflection loss between the external environment and the shield
- the skin depth of the conductor which is related to the frequency of the noise signal
- the multiple reflections of the signal inside the conductor.

From this analysis, the shield is more effective if d is greater than the skin depth, and the conductivity of the shield material is chosen as good as possible. The shielding effectiveness increases with the frequency. This shielding description could be flawed when the conductor is not infinite in one dimension and seams begin to play a role.

2.5.2 Transfer impedance

2.5.2.1 Definition

In terms of current, the E or H-field at the left-hand side of the shield (in figure 2.5) impresses a current over the infinite conductor. This current is called I_{CM} for the cylindrical shield in figure 2.6. The energy transferred inside the cable also induces currents over the centre conductor. As a result, a differential mode (DM) voltage appears across the impedance connected to the cable. The ratio of the voltage V_{DM} to the CM current I_{CM}, in (2.1), defines the transfer impedance (Z_T) of the cable [14, 17, 18].

$$Z_T = \frac{V_{DM}}{I_{CM}} \tag{2.1}$$

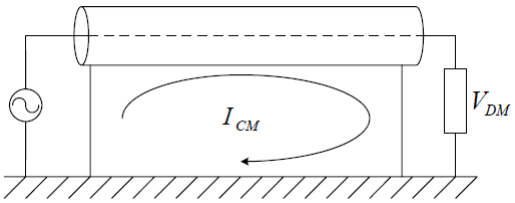

Figure 2.6: Transfer impedance in terms of DM voltage and CM current

2.5.2.2 Tubular Shielded Cable Model

To begin our understanding of transfer impedance, let us consider a coaxial cable made of a solid, thin and homogeneous shell. Due to the absence of holes over the cylindrical metallic sheath, the noise reaches the centre conductor from wave diffusion through the shield only. Schelkunoff investigated the transfer impedance of such a cable in 1934. This is given in (2.2) as a function of the inner radius a, the direct current (DC) resistance R_{dc}, the thickness d and the skin depth δ of the shield [7, 14, 19]. For this model, the current flows in the cable axis direction due to the homogeneity of the metallic sheath [12].

$$Z_d = R_{dc}\frac{(1+j)t/\delta}{sinh[(1+j)t/\delta]} \tag{2.2}$$

where

$$R_{dc} = \frac{1}{2\pi\sigma ad} \tag{2.3}$$

At low frequency, the thickness t is smaller than the skin depth δ. The highest transfer

impedance value that the pipe can provide to oppose the current is the DC resistance R_{dc}. Conversely, at high frequency, the current tends to circulate in the upper region of the shield. Less metal is involved in the current circulation. Z_d decreases and is given by:

$$Z_d = 2\sqrt{2}R_{dc} \cdot \frac{t}{\delta} \cdot e^{-(t/\delta)} \tag{2.4}$$

2.5.2.3 Tubular Shielded Cable With Apertures Model

More than the wave diffusion through the tube, the existence of apertures in the shield makes the penetration of both E and H-field in the internal region of the cable easier. It is clear from figure 2.7 that a perfectly symmetrical shield, carrying a uniformly distributed current I_S, creates no interference from magnetic coupling at the centre conductor. Because the currents induced by each pair of symmetrical points, such as M and N in figure 2.7, cancels. In figure 2.8, the H and E-field lines showing the fields' penetration through one hole is described. Once inside the cable, these fields induce an additional noise on the centre conductor. The transfer impedance of the cable becomes:

$$Z_T = Z_d + j\omega M_{12} \tag{2.5}$$

where M_{12} will be shown to incorporate both H and E-field coupling in figure 2.8

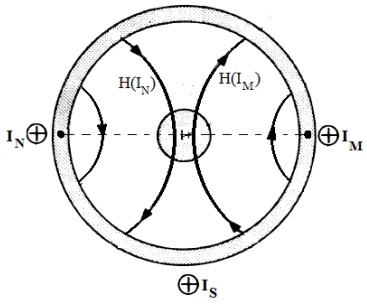

Figure 2.7: H-field lines at the centre conductor of a perfectly symmetrical shield created by two symmetrical current oriented in the same direction

a) Expression of the real part

Z_d represents the diffusion contribution developed by Schelkunoff in (2.2).

b) Expression of the mutual inductance M_{12}

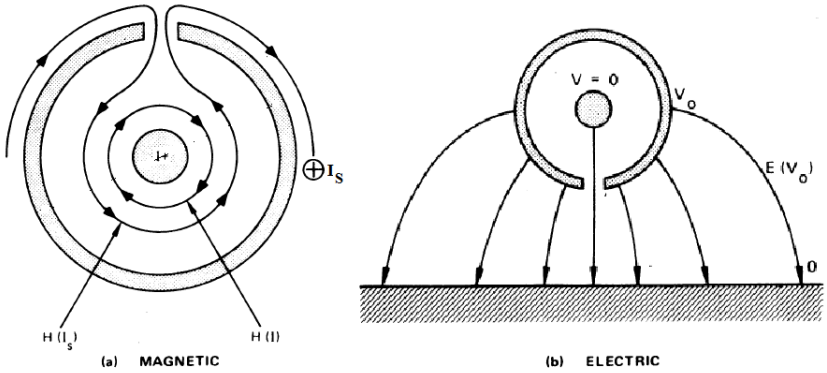

Figure 2.8: Penetration of (a) the E-field and (b) H-field inside the coaxial cable through an aperture localised on the shield [20]

When the wavelength of the incident signal is larger than the size of the aperture, the diffraction condition for a small source is met [21]. Here, the wave penetration through the hole can be modelled as electric and magnetic dipole moments $\vec{P_a}$ and $\vec{M_a}$ [7]. $\vec{P_a}$ is perpendicular to the aperture. Its magnitude varies proportionally with the E-field normal to the aperture plane. $\vec{M_a}$ lies in the aperture surface. Its magnitude varies with the tangential H-field.

Using this approach, Kaden and Marcuvitz developed the relationship between the external and internal region of the cable, in terms of polarizability of the hole, as follows [19, 20].

$$M_{12} = n\frac{\mu_0 \alpha_m}{\pi^2 D^2} \tag{2.6}$$

where: α_m is the magnetic polarizability of the aperture, D is the diameter of the shield, and n is the number of apertures per unit length of the cable.

For some test fixtures, such as a reverberation chamber, both electric and magnetic coupling occur at the same time. The magnetic polarizability α_m in (2.6) is replaced by the effective magnetic polarizability α_{meff} in (2.7) to account for both E and H-field coupling [22].

$$\alpha_{meff} = (1 + \frac{\alpha_e}{\alpha_m})\alpha_m \tag{2.7}$$

Where α_e and α_m are the electric and the magnetic polarizabilities of the apertures. The expressions of these parameters were derived in [7] and are summarised in appendix A for circular and elliptic holes.

2.5.2.4 Braided Shield Model

Two major concepts concerning the fields coupling on coaxial cable have been developed by engineers to model the inhomogeneity and the complexity of the braid. The first was presented by Vance in 1974. The second is based on Tini's model which has been improved by other engineers, such as Sali [11], through the years.

a) Characterisation of The Braid

The braided shield weaving geometry can be characterised, as illustrated in figure 2.9, in terms of: the radius a of the metallic sheath, the number of strand C in the braid, the wire diameter d, the conductivity σ of the shield material and the pitch angle α.

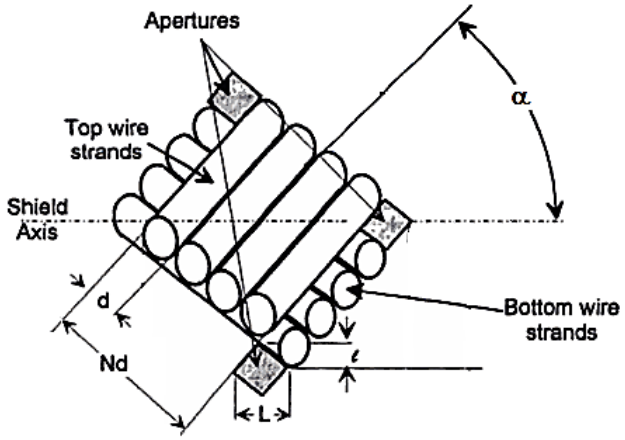

Figure 2.9: The weave parameters of a braided shield according to [7]

From these parameters, the fill factor F, the optical coverage K and the number of holes per unit length of the braid n are defined as follows [7, 20]:

$$F = \frac{NCd}{4\pi a cos(\alpha)} \tag{2.8}$$

$$K = 2F - F^2 \tag{2.9}$$

$$n = \frac{4\pi a sin(\alpha) cos(\alpha)}{N^2 d^2} F^2 \tag{2.10}$$

b) Vance's Model

Following the analysis of Schelkunoff, Kaden and Marcuvitz, Vance approximated the coupling on braided shield cable in the same manner as the coupling on a perforated tubular shield discussed in section 2.5.2.3 [20]. He assumed that the current flows

longitudinally over the braid. So, his model takes into account the coupling from the diffusion mechanism and the noise penetration through apertures only. The transfer impedance of the braided cable is similar to the equation stated in (2.5).

According to Tesche et al. [7], Vance's Model gives good results at low frequency, for $d << \delta$, and is accurate within a factor of 3 or less at high frequencies when $Z_T = j\omega M_{12}$.

For the diffusion part, obviously the woven construction of the braid influences the DC resistance of the shield because, a higher braid angle leads to more wire turns (more copper). Thus, accounting for the braid parameters, Vance defined the equivalent tubular shield DC resistance of the braid as follows

$$R_{dc} = \frac{4}{\pi d^2 NC\sigma cos(\alpha)} \tag{2.11}$$

By analogy with the Schelkunoff assumption, the approximated diffusion term is given by the following expression

$$Z_d = R_{dc}\frac{(1+j)d/\delta}{sinh[(1+j)d/\delta]} \tag{2.12}$$

For the aperture coupling, Vance approximated the rhombic holes created in-between the overlapping carriers by ellipses of eccentricity e [7, 20]. We can see from figure 2.10 that the orientation of the ellipse changes with the weave angle α. It is parallel to the cable axis if $\alpha < 45°$ and perpendicular if $\alpha > 45°$.

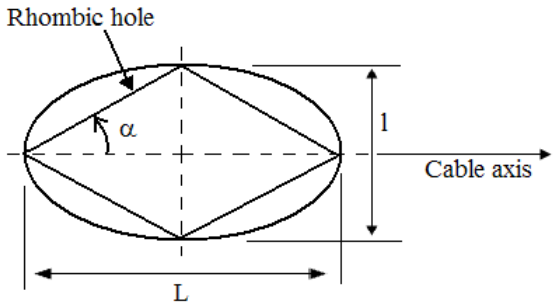

Figure 2.10: Elliptical approximation of the braid aperture

Using the expression of the number of holes per unit length of the braid n in (2.10) and the aperture polarizability of an ellipse [7] (see appendix A), we obtain the mutual coupling M_{12} of the cable as follows

$$M_{12}(H/m) \approx \begin{cases} \dfrac{\pi\mu_0}{6C}(1-K)^{3/2}\dfrac{e^2}{E(e)-(1-e^2)K(e)} & \alpha < 45° \\ \dfrac{\pi\mu_0}{6C}(1-K)^{3/2}\dfrac{e^2/\sqrt{1-e^2}}{K(e)-E(e)} & \alpha > 45° \end{cases} \tag{2.13}$$

where K is the optical coverage of the braid in (2.9), e represents the eccentricity of the aperture, $K(e)$ and $E(e)$ are the complete elliptical integrals given in appendix A.

c) Tini's Model

According to Tini, the current direction is not parallel to the cable axis for a braided shield. It follows the wires in a helix-like manner. Due to this current behaviour, following the wire alternatively inside and outside the shield (called porpoising [7]), an extra coupling occurs between the inner and the outer braid layers. A verification of this characteristic is reported by Tiedmann in [12]. Tini's formulation improved the braided shield model of Vance by inserting a third term in the transfer impedance expression in (2.5) as follows

$$Z_T(\Omega/m) = Z_d + j\omega M_{12} \pm j\omega M_b \tag{2.14}$$

The diffusion and the aperture coupling effects remain the same as developed by Vance in (2.12) and (2.13). However, the porpoising inductance M_b is given by equation (2.15) [7, 11]. The $\pm$ sign in (2.14) is introduced to account for the in-phase and out-of-phase contributions the inductive loops, made by the braid strands, contribute to the coupling [11].

$$M_b(H/m) = \frac{\mu_0 h}{4\pi D}(1 - tan^2\alpha) \tag{2.15}$$

with

$$h = \frac{2d}{1+\frac{w}{d}} \tag{2.16}$$

where h denotes the effective distance between the two layers of braid, D represents the outer diameter of the braid, d is the wire diameter and w is the mean distance between two carriers.

As far as h is concerned, it has been discussed and improved by Sali in [11]. Sali

demonstrated that Tini's expression of h in (2.16) overestimates the flux area between the braid layers [7]. He proposed a new expression and found more accurate results with experimental values [7, 11].

2.5.2.5 Z_T Behaviour with Frequency

a) Magnitude

For a very low frequency, Z_T is constant, dominated by the diffusion term R_{DC}. It decreases when the frequency becomes larger. The analytical expressions of Z_T, in (2.5) and (2.14), shows a linear variation of transfer impedance with frequency ($Z_T = j2\pi FM$) at high frequency. This infers a theoretical maximum transfer impedance slope of 20 dB/decade for a perforated pipe and a single braided coaxial cable at high frequency. A typical transfer impedance variation is presented in figure 2.11.

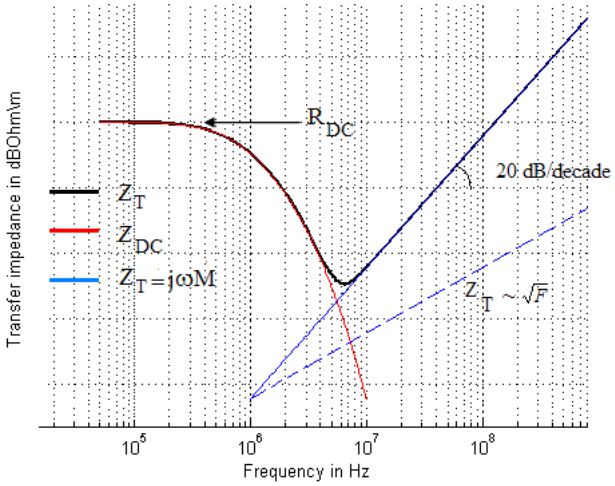

Figure 2.11: Typical transfer impedance variation

According to Tini, the experimental Z_T data of some coaxial cables shows sometimes a variation less than the predicted slope of $20dB/decade$ [7]. He noticed a trend proportional with $\sqrt{F}$ of the absolute Z_T curve. Later, he tried to improve his model using a porpoising inductance $M_b^{'}$ varying with $\sqrt{F}$ (equation (2.17)). Demoulini also noticed this variation in his work and proposed an additional term proportional to $\sqrt{F}$. He found that the $\sqrt{F}$ variation is a typical trend of cables with an optical coverage very close to 1. [7].

$$M_b^{'} = M_b(1 + \frac{a}{\sqrt{j\omega}}) \tag{2.17}$$

where a is a parameter depending on the cable construction. No analytical expression was specified by Tini concerning this parameter.

b) Phase θ

The phase (θ) of Z_T is 0° at low frequency for each model. If Z_{DC} is very small compared to $j\omega M$ at high frequency, it increases up to 90° for Vance's model. Conversely, it lies between −90° and +90° for Tini's model. For the later case, three possibilities exist:

- if $\theta < 0$ ($M_{12} < M_b$), the coupling is dominated by the porpoising term
- if $\theta > 0$ ($M_{12} > M_b$), it is dominated by the field penetration through apertures
- if $\theta = 0$ ($M_{12} = M_b$), cancellation between the two terms occurred

According to the phase variation of Tini's model, equation (2.14), it is possible to manipulate the braid configuration which lowers the term $j\omega(M_{12} \pm M_b)$ to optimise Z_T [11].

2.6 Coaxial Cable Shielding Evaluation

2.6.1 RFI Sources Identification: MeerKAT Case

For the MeerKAT interferometer project, especially the phase-2, each telescope receives the signal from the universe from 580 MHz to 1.015 GHz [1]. Thereafter, a chain of equipment placed inside the pedestal of each telescope, connected by coaxial cables, collects and transmits the data to a correlator which manages the telescopes array. Two major RFI sources can be identified from this general description of the MeerKAT system. At first, the coaxial cables might be exposed to the man-made radiation from the surrounding region. These cables are also subjected to the system self-generated.

According to the Z_T curve presented in section 2.5.2.5, the low and high frequency signals are potential sources of interference due to the high value of the cable Z_T for these frequencies. Considering these facts, it becomes clear that the Z_T investigation should be realised from the lowest frequency as possible. Furthermore, the frequency range must include the MeerKAT phase-2 working frequencies.

2.6.2 Methodology Selection

A wide variety of test methods exists for screening effectiveness evaluation and a summary of the main characteristics of these approaches are provided in [23]. We are particularly interested on the reverberation chamber (RC) technique, because the RC measurement is not length-dependent and the worst case is easily detectable. This is generally caused

by the ability of the chamber to generate a uniform fields within its working volume [24]. The RC technique is, however, suitable for high frequency applications up to 40 GHz [23]. Thus, a second method is necessary for the characterisation of the Z_T low frequency part.

The setup proposed by Benson et al. in [5, 17], known as the current injection or the field to wire method, is chosen due to its simplicity (see figure 2.13) and most importantly it is a non-invasive technique. This allows a rapid measurement of cables' Z_T without damaging the CUT.

All the important stages for the wideband Z_T characterisation is shown in figure 2.12.

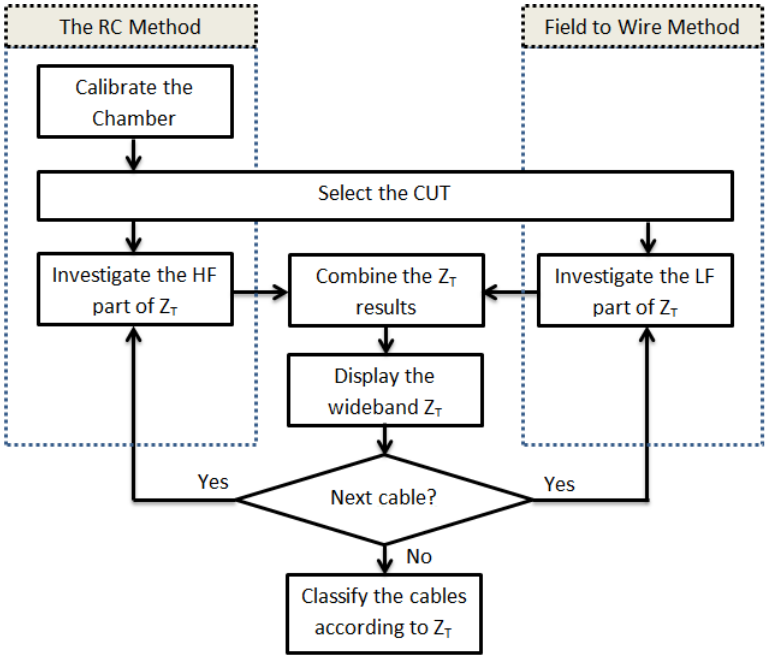

Figure 2.12: Z_T classification process overview

2.6.3 Measurements Specifications

2.6.3.1 The Reverberation Chamber Method

With the RC technique, the CUT is placed inside a uniform EM field generated by an antenna located inside the chamber. The CUT acts like an antenna and couples to the surrounding energy through the process described in section 2.3.1. The ratio between the power received by the cable (P_{Cut}) and the power injected inside the chamber (P_{Ref}) gives the SE of the CUT as follows:

$$SE = \frac{P_{Cut}}{P_{Ref}} \tag{2.18}$$

Equation (2.18) can be expressed in terms of the injected power (P_{Inj}) and the insertion loss IL of the chamber as well. In this case, we have:

$$SE(dB) = -10 \cdot log(\frac{P_{Cut}}{P_{Inj}}) - IL \tag{2.19}$$

From the SE measurement, we compute the Z_T of the CUT using the expression of Eicher and Boillot between SE and Z_T [22, 25]. For a single hole leakage, such as a perforated coaxial air-line, this correlation is given by (2.20).

$$Z_{tot}^2 = Z_T^2 + Z_f^2 = 2Z_1Z_2 10^{-SE/10} \tag{2.20}$$

and for a cable with multiple leakages such as a braided screen:

$$Z_{tot}^2 = \frac{2Z_1Z_2 \cdot 10^{-[SE+S(D/\lambda)]/10}}{D^2} \tag{2.21}$$

here D is the length of the coupling area and $S(D/\lambda)$ is the summing function of the infinitesimal coupling over the cable. $S(D/\lambda)$ is expressed as follows:

$$S(D/\lambda) = 10 \cdot log(\frac{1}{\pi}\int_0^{\pi} \left[\frac{sin[\frac{\pi D}{\lambda}(cos\phi - \sqrt{\varepsilon})]}{\frac{\pi D}{\lambda}(cos\phi - \sqrt{\varepsilon})}\right]^2 d\phi) \tag{2.22}$$

where ε represents the relative permittivity of the dielectric support in the CUT.

2.6.3.2 The Field to Wire Technique

The current injection method of Benson et al. [5] uses two current probes and a metallic plate to support the CUT as shown in figure 2.13. Here, the brass board, the two L-plates and the cable braid form a loop which leads to a CM current creation. The setup is excited by the signal injected into CP_1. Thereafter, from the reading of the CP_2 output voltage (V_{CP}) and the DM voltage (V_{DM}) induced on the cable, we evaluate the CUT Z_T (see equation (2.23)).

$$Z_T = \frac{4Z_{CP}}{CF} \cdot \frac{V_{DM}}{V_{CP}} \tag{2.23}$$

In this expression, Z_{CP} is the Z_T of the current probe and CF is the correction factor of the setup in (2.24)

$$CF = \frac{\sqrt{\beta_c^2 C^2 + S^2}}{\beta_c^2 + \beta^2} \tag{2.24}$$

where β_c is the cable phase constant, β is the free-space phase constant and:

$$C = cos(\beta_c l) - cos(\beta l), \qquad S = \beta_c sin(\beta_c l) - \beta sin(\beta l)$$

Due to the electrical length l of the CUT, a standing wave appears on the setup when l is greater than $\lambda/4$.

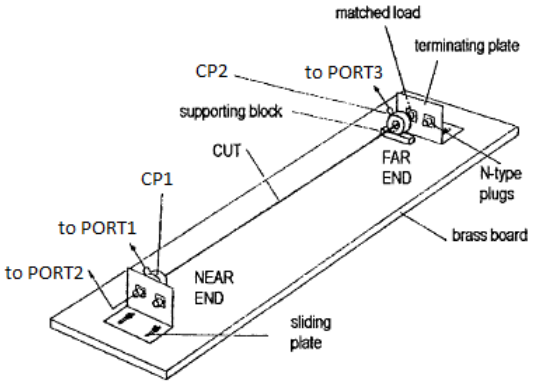

Figure 2.13: Current injection method setup according to Benson et al. [17, 5]

2.7 Summary

The external noise reaches the centre conductor of coaxial cables through the imperfections of the braid as reviewed in this chapter. At low frequency the Z_T is particularly dominated by a wave diffusion process inversely proportional to the frequency. At high frequency, the fields' coupling through the apertures and the porpoising of the braid takes over. The Z_T variation becomes linear at a rate of 20 dB/decade, but a variation of 10 dB/decade is also possible.

For an appropriate cable shielding evaluation of the MeerKAT project, a wideband Z_T is necessary. Two methods were selected for the Z_T investigation: the RC method, for the high frequency part, and the field to wire method of Benson et al. [5], for the low frequency part.

CHAPTER 3

Reverberation Chamber Characterisation

The RC technique is becoming more and more widespread in EMC testing due to its ability to generate a uniform and high field strength from a moderate input power [26]. Initially, it was used to investigate the electromagnetic absorption of materials. Later, wider applications have been found, such as the shielding effectiveness evaluation of cables, connectors and enclosures. Recently, it was applied in wireless system for antenna characterisation.

The knowledge of the RC concept is essential for an accurate application of the technique in our Z_T investigation. Here, two approaches are combined to understand the RC field uniformity principles. The first approach is based on waveguide and cavity resonator theory, for analytical comprehension of the subject. With the second approach, the IEC standard 61000-4-21, we determine a practical method for the characterisation of RCs.

3.1 Modal Analysis of Reverberation Chambers

A static RC is similar to a cavity resonator when the stirrers are not taken into account. We expect the EM signal enclosed inside the chamber to experience multiple reflections from the walls and to produce standing wave patterns (also called modes) in the inner region [27]. To determine the characteristics and RCs' mechanisms, let us investigate the fields' configuration inside the cavity resonator of figure 3.1.a.

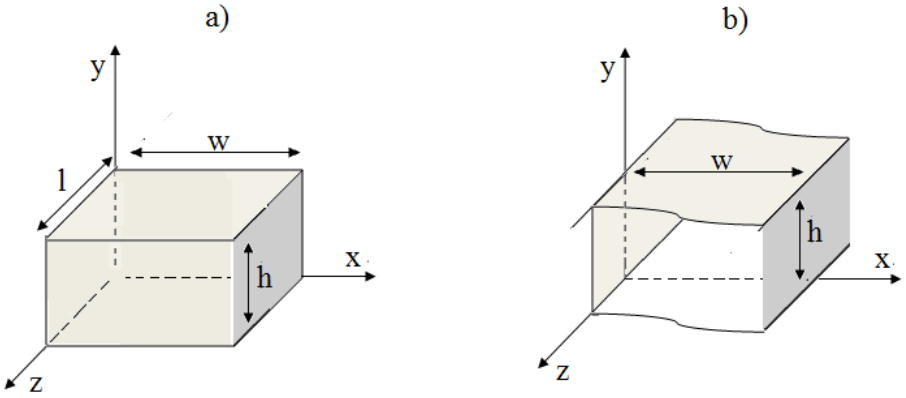

Figure 3.1: Description of a rectangular cavity resonator

In Cartesian coordinates, the fields inside the chamber verify Maxwell's equations. In phasor notation, the wave equations are:

$$\triangle \tilde{E} + \omega^2 \mu \epsilon \tilde{E} = 0 \tag{3.1a}$$

$$\triangle \tilde{H} + \omega^2 \mu \epsilon \tilde{H} = 0 \tag{3.1b}$$

Both forward and backward waves exist inside a cavity resonator, but to simplify the problem let us consider the forward propagation along the z axis of the waveguide in figure 3.1.b first. In this case, the E and H-field of the wave are in the forms [27]:

$$\tilde{\vec{E}}(x,y,z) = \tilde{E}_x(x,y)e^{-\hat{\gamma}z}\,\vec{e_x} + \tilde{E}_y(x,y)e^{-\hat{\gamma}z}\,\vec{e_y} + \tilde{E}_z(x,y)e^{-\hat{\gamma}z}\,\vec{e_z} \tag{3.2}$$

$$\tilde{\vec{H}}(x,y,z) = \tilde{H}_x(x,y)e^{-\hat{\gamma}z}\,\vec{e_x} + \tilde{H}_y(x,y)e^{-\hat{\gamma}z}\,\vec{e_y} + \tilde{H}_z(x,y)e^{-\hat{\gamma}z}\,\vec{e_z} \tag{3.3}$$

3.1.1 Longitudinal Fields Component

Equations (3.1a) and (3.1b) give respectively, for the z components of the fields, the following differential equations

$$\frac{\partial^2 \tilde{E}_z}{\partial x^2} + \frac{\partial^2 \tilde{E}_z}{\partial y^2} = -(\omega^2 \mu \epsilon + \gamma^2)\,\tilde{E}_z \tag{3.4a}$$

$$\frac{\partial^2 \tilde{H}_z}{\partial x^2} + \frac{\partial^2 \tilde{H}_z}{\partial y^2} = -(\omega^2 \mu \epsilon + \gamma^2)\,\tilde{E}_z \tag{3.4b}$$

Using the separation of variables method, we assume that the solutions of (3.4) are similar to the following expressions

$$\tilde{E}_z(x,y) = \tilde{X}(x)\tilde{Y}(y) \tag{3.5a}$$
$$\tilde{H}_z(x,y) = \tilde{R}(x)\tilde{S}(y) \tag{3.5b}$$

By substituting (3.5a) in (3.4a), we obtain

$$\frac{\partial^2 \tilde{X}(x)}{\partial x^2} + \tilde{X}(x)M^2 = 0 \tag{3.6a}$$
$$\frac{\partial^2 \tilde{Y}(y)}{\partial y^2} + \tilde{Y}(y)N^2 = 0 \tag{3.6b}$$

where M and N are constants satisfying to the relation

$$M^2 + N^2 = \omega^2\mu\epsilon + \gamma^2 \tag{3.7}$$

$\tilde{F} = C\, e^{jDx}$ is a typical solution of the second-order linear differential equation in (3.6a), where C and D are constants depending on the boundary conditions of the waveguide. Replacing $\tilde{X}(x)$ by $\tilde{F}$, (3.6a) gives

$$\tilde{X}(x) = C_1\, e^{jMx} + C_2\, e^{-jMx} \tag{3.8}$$

The same procedure is applied for (3.6b). This gives

$$\tilde{Y}(x) = K_1\, e^{jNy} + K_2\, e^{-jNy} \tag{3.9}$$

Hence, the longitudinal components of the fields in (3.5) become

$$\tilde{E}_z(x,y) = \left(C_1\, e^{jMx} + C_2\, e^{-jMx}\right)\left(C_3\, e^{jNy} + C_4\, e^{-jNy}\right)\, e^{-\hat{\gamma}z} \tag{3.10}$$
$$\tilde{H}_z(x,y) = \left(K_1\, e^{jMx} + K_2\, e^{-jMx}\right)\left(K_3\, e^{jNy} + K_4\, e^{-jNy}\right)\, e^{-\hat{\gamma}z} \tag{3.11}$$

3.1.2 x and y Field Components

Once the expressions of $\tilde{E}_z$ and $\tilde{H}_z$ are known, we can derive the x and y components of the fields using the first relation of Maxwell's equations ($\nabla \times \tilde{E} = -j\omega\mu\tilde{H}$). In terms of

$\tilde{E}_z$ and $\tilde{H}_z$, we have:

$$\tilde{E}_x = -\frac{1}{\hat{\gamma}^2 + \omega^2\mu\epsilon}\left(\hat{\gamma}\frac{\delta\tilde{E}_z}{\delta x} + j\omega\mu\frac{\delta\tilde{H}_z}{\delta y}\right) \tag{3.12a}$$

$$\tilde{E}_y = \frac{1}{\hat{\gamma}^2 + \omega^2\mu\epsilon}\left(-\hat{\gamma}\frac{\delta\tilde{E}_z}{\delta y} + j\omega\mu\frac{\delta\tilde{H}_z}{\delta x}\right) \tag{3.12b}$$

$$\tilde{H}_x = \frac{1}{\hat{\gamma}^2 + \omega^2\mu\epsilon}\left(-\hat{\gamma}\frac{\delta\tilde{H}_z}{\delta x} + j\omega\mu\frac{\delta\tilde{E}_z}{\delta y}\right) \tag{3.12c}$$

$$\tilde{H}_y = -\frac{1}{\hat{\gamma}^2 + \omega^2\mu\epsilon}\left(\hat{\gamma}\frac{\delta\tilde{H}_z}{\delta y} + j\omega\mu\frac{\delta\tilde{E}_z}{\delta x}\right) \tag{3.12d}$$

3.1.3 Boundary Conditions

Because the cavity resonator and the waveguide are bounded by metallic surfaces, the E-field is expected to be equal to zero at these areas. For the waveguide, this corresponds to $\tilde{E}_z(0, y, z) = \tilde{E}_z(w, y, z) = \tilde{E}_z(x, 0, z) = \tilde{E}_z(x, h, z) = 0$. For the cavity resonator, we have $\tilde{E}_z(0, y, z) = \tilde{E}_z(w, y, z) = \tilde{E}_z(x, 0, z) = \tilde{E}_z(x, h, z) = \tilde{E}_z(x, y, 0) = \tilde{E}_z(x, y, l) = 0$

3.1.4 Transverse Magnetic (TM) mode

The H-field lies in the transverse plane of the propagation (plane (x,y)) for the TM mode. We evaluate the constants of the E-field in (3.10) from the boundary conditions stated in previous section. The final solution of this calculation corresponds to the following expressions for the forward propagation.

$$\tilde{E}_z(x, y, z) = \hat{E}_{zm} sin(Mx) sin(Ny)\, e^{-\hat{\gamma}z} \tag{3.13}$$

$$\tilde{H}_z(x, y, z) = 0 \tag{3.14}$$

where $M = \frac{m\pi}{w}$, $N = \frac{n\pi}{h}$ and m, $n \in \mathbb{N}$

Accounting for the backward propagation, the z component of the E-field in the cavity resonator can now be written as

$$\tilde{E}_z(x, y, z) = \hat{E}^+_{zm} sin(Mx) sin(Ny)\, e^{-\hat{\gamma}z} + \hat{E}^-_{zm} sin(Mx) sin(Ny)\, e^{+\hat{\gamma}z} \tag{3.15}$$

The application of the boundary condition along the z axis of the cavity, $\tilde{E}(x, y, 0) =$

$\tilde{E}(x, y, l) = 0$, yields

$$\tilde{E}_z(x, y, z) = 2\hat{E}_{zm} sin(Mx) sin(Ny) cos(Pz) \tag{3.16}$$

where $P = \frac{p\pi}{l}$ and $p \in \mathbb{N}$

Substituting $\tilde{E}_z$ in (3.12) to its expression in (3.16), we obtain the following equations for the TM mode

$$\tilde{E}_z = 2\hat{E}_{zm} sin(Mx) sin(Ny) cos(Pz) \tag{3.17a}$$
$$\tilde{E}_x = -\frac{2MP}{M^2 + N^2} \hat{E}_{zm}\, cos(Mx) sin(Ny) sin(Pz) \tag{3.17b}$$
$$\tilde{E}_y = -\frac{2NP}{M^2 + N^2} \hat{E}_{zm}\, cos(Mx) cos(Ny) sin(Pz) \tag{3.17c}$$
$$\tilde{H}_x = \frac{j2\omega\epsilon N}{M^2 + N^2} \hat{E}_{zm}\, sin(Mx) cos(Ny) cos(Pz) \tag{3.17d}$$
$$\tilde{H}_y = -\frac{j2\omega\epsilon M}{M^2 + N^2} \hat{E}_{zm}\, cos(Mx) sin(Ny) cos(Pz) \tag{3.17e}$$
$$\tilde{H}_z = 0 \tag{3.17f}$$

3.1.5 Transverse Electric (TE) mode

For the TE mode, the E-field lies in the transverse plane of the propagation ($\tilde{E}_z = 0$). In this case, (3.12a) and (3.12b) can be rewritten as follows

$$\tilde{E}_x = -\frac{j\omega\mu}{\hat{\gamma}^2 + \omega^2\mu\epsilon} \left(\frac{\delta \tilde{H}_z}{\delta y} \right) \tag{3.18}$$
$$\tilde{E}_y = \frac{j\omega\mu}{\hat{\gamma}^2 + \omega^2\mu\epsilon} \left(\frac{\delta \tilde{H}_z}{\delta x} \right) \tag{3.19}$$

where $\tilde{H}_z$ corresponds to the expression in (3.11).

Similar to the approach used for the TM mode, we determine the constants of the H-field from the E-field boundary conditions. The combination of both forward and backward wave equations gives the following solution for the H-field z component.

$$\tilde{H}_z(x, y, z) = -2j\hat{H}_{zm} cos(Mx) cos(Ny) sin(Pz) \tag{3.20}$$

where $P = \frac{p\pi}{l}$ and $p \in \mathbb{N}$

Thereafter, with (3.20) and (3.12), we obtain

$$\tilde{H}_x = j\frac{2MP}{M^2+N^2}\hat{H}_{zm}\, sin(Mx)cos(Ny)cos(Pz) \tag{3.21a}$$

$$\tilde{H}_y = j\frac{2NP}{M^2+N^2}\hat{H}_{zm}\, cos(Mx)sin(Ny)cos(Pz) \tag{3.21b}$$

$$\tilde{H}_z = -2\hat{H}_{zm}cos(Mx)cos(Ny)sin(Pz) \tag{3.21c}$$

$$\tilde{E}_x = \frac{2\omega\mu N}{M^2+N^2}\hat{H}_{zm}\, cos(Mx)sin(Ny)sin(Pz) \tag{3.21d}$$

$$\tilde{E}_y = -\frac{2\omega\mu M}{M^2+N^2}\hat{H}_{zm}\, sin(Mx)cos(Ny)sin(Pz) \tag{3.21e}$$

$$\tilde{E}_z = 0 \tag{3.21f}$$

3.2 Stirred Chamber Properties

The E-field pattern in the inner region of our RC ($2,455m \times 2,475m \times 3,72m$) is shown in figure 3.2, for a single frequency (the TM mode F_{212}), to illustrate the previous analysis. A second figure displaying the E-field pattern according to the stirrer's rotation is presented in figure 3.3. This last figure corresponds to the FEKO simulation results made by Nijenhuis of their RC for four stirrer positions [28].

In figure 3.3, we clearly see that the field's maximum is no longer oscillating at one given location as in figure 3.2, but it moves across a specific area of the central region. The stirrer's rotation changes then the boundary conditions of the chamber. This reshapes the E-field standing wave pattern inside the cavity resonator. If we can delimit the field's fluctuation area, a DUT placed within this volume would be exposed to the same maximum, minimum and average E-field over time [26, 29]. The chamber is qualified to be able to provide a statistically uniform environment, for EMI and EMS testing, when the wave fluctuation is kept within a prescribed limit for a given number of stirrer positions [26, 29]. More concerning the characterisation of the field uniformity is provided in section 3.4.5

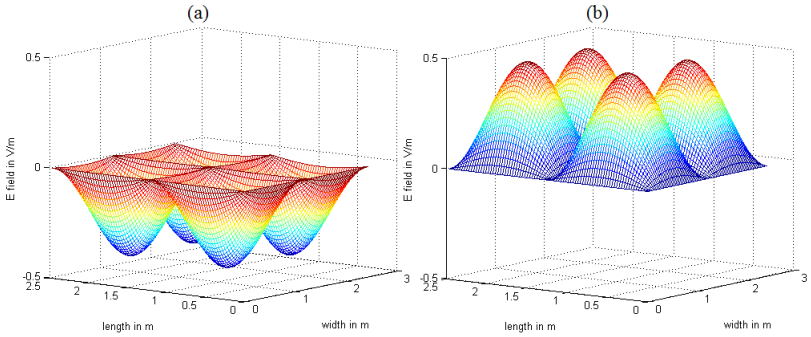

Figure 3.2: E-field pattern for the TM mode F_{212}. (a) at $80ns$. (b) at $90ns$

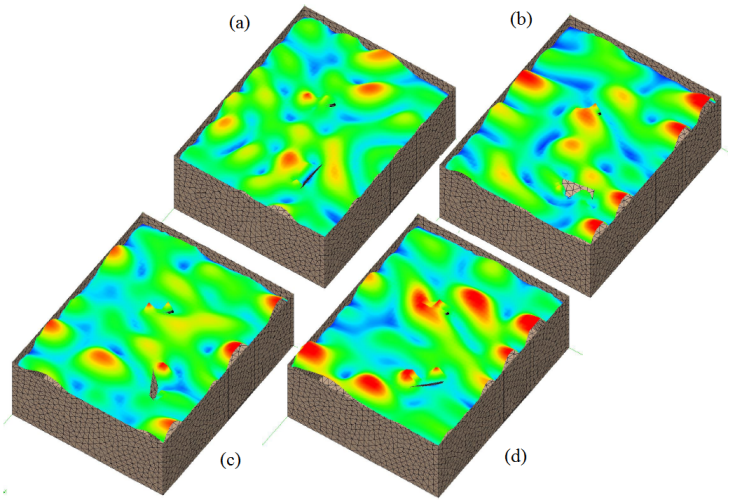

Figure 3.3: FEKO simulation results, from [28], of the E-field pattern at 200 MHz with respect to the stirrer's position. (a) Position 1($angle = 7.2°$), (b) Position 15($angle = 108°$), (c) Position 30($angle = 216°$), (d) Position 45($angle = 324°$)

3.3 Reverberation Chamber Characteristics

3.3.1 Static Chamber

Following the waveguide and cavity resonator analysis, the static chamber is characterised by its cut-off frequency, its resonant frequency and the number of modes the chamber can produce. The number of modes is particularly important because the higher the modes generated inside the chamber, the higher the probability of exposing the DUT to the same mean E-field. This is the principal reason why a RC is appropriate for high frequency measurements. In terms of frequency and the size of the chamber, the total possible number of modes within the chamber is given by

$$N(f) = \frac{8\pi}{3} wlh \left(\frac{f}{c}\right)^3 - (w + l + h)\frac{f}{c} + \frac{1}{2} \tag{3.22}$$

The wave is not propagating inside the cavity according to (3.17) and (3.21), or the E-field distribution in figure 3.2. So, the condition in (3.7) becomes

$$M^2 + N^2 = \omega^2 \mu\epsilon - P^2 \tag{3.23}$$

This gives the following resonant frequency for both TM and TE modes

$$F_{mnp} = \frac{1}{2\sqrt{\mu\epsilon}} \sqrt{\left(\frac{m}{w}\right)^2 + \left(\frac{n}{h}\right)^2 + \left(\frac{p}{l}\right)^2} \tag{3.24}$$

where m, n and $p \in \mathbb{N}$

Hence, the cut-off frequencies of the two modes are

$$\begin{aligned} F_{110} &= \frac{1}{2\sqrt{\mu\epsilon}} \sqrt{\left(\frac{1}{w}\right)^2 + \left(\frac{1}{h}\right)^2} \quad \text{TM mode} \\ F_{101} &= \frac{1}{2\sqrt{\mu\epsilon}} \sqrt{\left(\frac{1}{w}\right)^2 + \left(\frac{1}{l}\right)^2} \quad \text{TE mode} \end{aligned} \tag{3.25}$$

3.3.2 Dynamic Chamber

When the stirrer's rotation is taken into account, additional characteristics of the chamber arise.

3.3.2.1 Field Uniformity and Working Volume

The most important characteristic which differentiates an ordinary enclosure to a RC is its ability to generate a uniform field level within a certain volume of the room, called the working volume. For a rectangular RC, this region is typically defined within a distance of $\lambda/4$ from the walls and any metallic structures such as the stirrers [24].

3.3.2.2 Lowest Usable Frequency

Accordingly, a new lowest usable frequency (LUF) should be defined regarding the field uniformity effectiveness within the working volume. From this fact, different definitions of

the LUF exist depending on the definition of the field uniformity. For the IEC standard in [24], it is slightly above three times the first chamber resonance. However, only from practical examination (calibration measurement) that we can find the LUF exact value due to the dependence between the field uniformity and the tuner efficiency of the chamber [24].

3.3.2.3 Isotropy

The fields inside a RC are constantly reflected in all directions by the stirrer during one rotation. All possible wave polarisations are present in the working volume for an ideal RC. Consequently, the orientation of any devices placed within the working volume, such as the DUT or the antenna used for the measurement, becomes irrelevant [24].

3.3.2.4 Field Statistics

The fields' distribution inside a RC constitutes the basis of the statistical uniformity analysis concept outlined in the IEC standard. It maps the probability of the random variables E-field and H-field to take all possible values of the fields inside the chamber. According to Bäckström and Per-Simon Kildal in [29], the real and imaginary parts of the E and H-field are normally distributed around the mean for a well-stirred chamber. The magnitude of the rectangular components of the field follows a chi-distribution with two degrees of freedom. Hence, the power received by a general antenna, which is related to the square of the magnitude, fits a chi-squared distribution with two degrees of freedom [24, 29].

3.4 IEC 61000-4-21 Standard Calibration

The calibration of a RC is a series of measurements for examining the chamber characteristics such as the signal attenuation and the E-field uniformity in the working volume. This should be performed once for an empty chamber before using the facility. Also, it should be repeated if major modifications are done, such as: stirrer replacement, use of absorbers, metallic coating improvement of the wall, etc.

3.4.1 Measurement Stirring Mode

The measurement with the RC is generally performed during one rotation of the tuner because the field pattern repeats after each stirrer revolution. This requires a good coordination between the measurement and the stirrer to avoid measuring the same thing. For the IEC 61000-4-21 standard, two operations can be used.

For the first case, called mode-tuned operation, the stirrer is set at a fixed location while the frequency is swept over the frequency range. Afterwards, the tuner is moved to the next angle position and the same process is repeated until completion of a full rotation of N_S positions.

For the second case, called mode-stirred operation, the stirrer is set to rotate freely while the signal is kept inside the chamber during one full rotation. A set of N_S measurements are performed during this time, for each frequency, before moving on to the next frequency point.

At the end of the measurement, N_S samples are obtained for each frequency. These data are averaged for the investigation of the mean E-field produced in the working volume. Clearly, the higher the number of samples (N_S) taken per revolution the accurate the field average.

3.4.2 Calibration Procedure

Eight receiver positions are necessary for the calibration of the chamber. These points are located near the eight corners of the working volume as shown in figure 3.4. Due to the fact that the working volume reaches nearly to the wall when the frequency increases (see section 3.3.2.1), the eight locations should be related to the smallest working volume. A good option is the placement of the receiver far enough from the wall using the first resonance of the chamber as a LUF reference.

During the calibration, a signal of known power is injected into the chamber at a fixed location within the working volume. Both of the stirring mode presented in section 3.4.1 can be used to collect the eight radiated powers at the eight corners. But, before doing the measurement, the source should not pointed towards the receiver to prevent direct coupling between them.

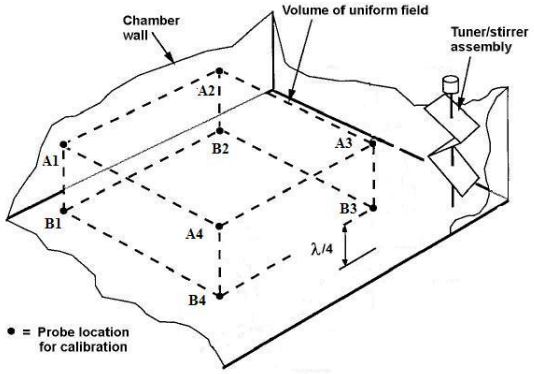

Figure 3.4: Recommended locations for the calibration of the RC [24]

3.4.3 Parameters of interest

3.4.3.1 Chamber Attenuation

Throughout the reflections of the signal from the walls and the stirrers, some part of the injected energy is absorbed by the chamber. So, the first parameter we derive from the calibration measurement is the attenuation caused by the chamber on the input signal. It is given by the following expression

$$Att_{Ch} = \left\langle \frac{P_{Rx}}{P_{Tx}} \right\rangle_{N\ probe-positions} \tag{3.26}$$

where P_{Rx} represents the received power at the probe position and P_{Tx} is the power radiated by the transmitting antenna. If P_{Rx} is equal to the maximum received power in one revolution, the attenuation is called antenna calibration factor (ACF). If it is evaluated from the average received power in one revolution, it is named the chamber insertion loss (IL)

3.4.3.2 Chamber Mean E-field

The second parameter we calculate from the calibration data is the average E-field within the working volume. Frequently, an antenna is used for the measurement of P_{Rx} at the eight locations. In this case, the maximum mean E-field (E_{max}) is given by

$$E_{max} = \left\langle \frac{8\pi}{\lambda} \sqrt{5 \frac{P_{MaxRx}}{\eta_{Rx}}} \right\rangle_{N\ probe-positions} \tag{3.27}$$

where P_{MaxRx} is the maximum received power over one revolution of the tuner and η_{Rx} is the efficiency factor of the receiving antenna (assumed to be 0.75 for a log periodic dipole array (LPDA) antenna and 0.9 for a horn antenna).

Concerning the average E-field. the formulation derived by Ladbury and Koepke in (3.28) [30] will be used.

$$E_{mean} = \sqrt{\frac{\langle P_{Rx} \rangle\, 8\pi\eta}{\lambda^2}} \cdot \frac{15}{16} \cdot \sqrt{\frac{\pi}{3}} \cdot \frac{\Gamma(3N)\sqrt{3N}}{\Gamma(3N + 1/2)} \tag{3.28}$$

where $\Gamma(X)$ is the factorial function evaluated at X and η is the wave impedance in free-space

3.4.4 Chamber Loading Factor CLF

In general, when a DUT is placed in the working volume for a test, the internal environment of the chamber is affected by its size [24]. It changes the fields' distribution inside the room and the attenuation factor derived from the empty chamber calibration. The DUT effect can be determined, using the loading factor in (3.29), by recalibrating the chamber in the presence of the DUT within the working volume. A new attenuation, called the chamber calibration factor (CCF), is computed from this new measurement. This gives the loading factor of the chamber as follows

$$CLF = \frac{CCF}{ACF} \tag{3.29}$$

3.4.5 Field Uniformity Validation

The chamber meets the field uniformity requirement of the IEC 61000-4-21 standard if the standard deviation of the maximum E-field is within 3 dB above 400 MHz, 4 dB at 100 MHz decreasing linearly to 3 dB at 400 MHz, and within 4 dB below 100 MHz.

From the calibration data, we calculate the eight E-fields at the eight corners of the working volume using (3.27). Thereafter, we evaluate the standard deviation of the eight maximum

E-field and compare it to the IEC requirements for the uniformity. From this comparison, we determine the frequency range of the uniformity and the LUF of the chamber.

The standard deviation (in dB) of the E-field is given by

$$\sigma(dB) = 20 \cdot log_{10}\left(\frac{\sigma + E_{max}}{E_{max}}\right) \tag{3.30}$$

where σ is the linear standard deviation of the E-field and E_{max} is the estimated E-field in (3.27).

3.5 E-field Uncertainty

3.5.1 Stirrer Efficiency

The uncertainty quantification depends primarily on the stirrer efficiency of the chamber. Before its evaluation, we need to know how efficient is the stirrer. In general, it is related to the number of independent samples N_{Ind} the stirrer can provide. The higher N_{Ind}, the efficient the stirrer and the better the uncertainty. Thus, the determination of N_{Ind} among the number of samples N_S collected over one rotation must be known for the uncertainty evaluation [24].

It is clear that for a small value of N_S, all the samples might be all independent ($N_{Ind} = N_S$). However, to achieve a good uncertainty, we have to reach the maximum N_{Ind} the stirrer is able to provide. This is only possible by oversampling the measurement using a large number of samples per revolution [31].

From the sequence of data X with N_S values, we can estimate N_{Ind} using the autocorrelation coefficient ρ in (3.31) [24, 32, 33, 34]. ρ varies between $[-1, 1]$, where -1 and 1 corresponds to a complete correlation, and 0 to a completely uncorrelated data [34]. According to the standard [24], the data is regarded as uncorrelated when $|\rho| \leqslant 0.37$.

$$\rho_i = \frac{Cov(X, Y_i)}{\sqrt{Var(X) \cdot Var(Y_i)}} \tag{3.31}$$

In (3.31), Y is obtained by shifting the values of X by i position to the right

$$\begin{aligned} if \quad & X = [E_1, E_2, ..., E_{N_S-1}, E_{N_S}] \\ & Y_1 = [E_{N_S}, E_1, E(2), ..., E_{N_S-1}] \\ & Y_2 = [E_{N_S-1}, E_{N_S}, E(1), ..., E_{N_S-2}] \\ & \vdots \end{aligned}$$

The terms 'Cov' and 'Var' denote respectively the covariance and variance of the random variables X or Y_i.

A typical plot of the correlation coefficient ρ is shown in figure 3.5 with the offset Δ from where the correlation is lost ($|rho| > 0.37$). Once Δ is known, N_{Ind} is derived using (3.32) [24, 31]

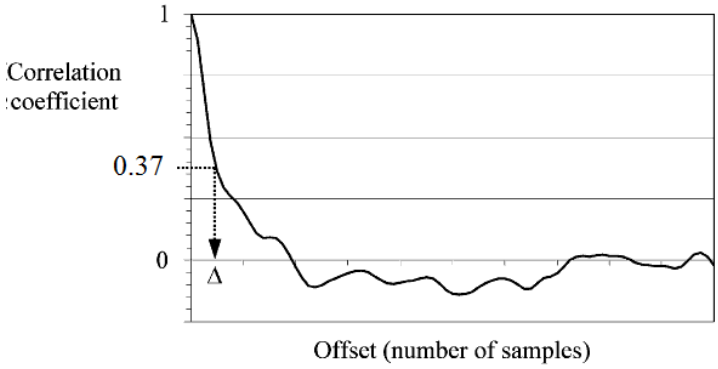

Figure 3.5: Typical autocorrelation result and the offset Δ at which the correlation is lost [31]

$$N_{Ind} = \frac{N_S}{\Delta} \tag{3.32}$$

3.5.2 Confidence Interval

For N_{ind} independent positions of the stirrer, the confidence interval d (in dB) of the field is given by [33, 35]

$$d = 10 \cdot log_{10} \frac{1 + k/\sqrt{zN_{ind}}}{1 - k/\sqrt{zN_{ind}}} \tag{3.33}$$

where k denotes the level of confidence ($k = 1.96$ for 95%) and z is the number of dimension of the field data (1 or 3) [35].

We can also find from (3.33) the number of independent samples corresponding to a chosen level of confidence. For this situation, we have

$$N_{Ind} = \frac{k^2}{z}\left(\frac{10^{d/10}+1}{10^{d/10}-1}\right)^2 \tag{3.34}$$

3.6 OATS E-field Equivalent Estimation

Over the years, the open area test site (OATS) facility has been, and still is, the engineers' first option for EMC radiated emission testing [36]. Usually, it is located far away from the EMI of a town. This makes the OATS the appropriate place for a full standards compliance evaluation. But, it can not be done frequently since it is known as costly to setup and weather-dependent. An alternative low-cost method, such as the RC, has to be used for pre-compliance testing [36, 37].

The RC method does not perform a direct measurement of the OATS E-field. Instead, it measures the total radiated power from the EUT using one of the expressions in (3.35) or (3.36). Afterwards, the OATS E-field equivalent radiated in free-space or half-space conditions is estimated using (3.37) or (3.38).

$$P_{Radiated} = \frac{P_{av}\cdot\eta_{Tx}}{CCF} \tag{3.35}$$

$$P_{Radiated} = \frac{P_{Max}\cdot\eta_{Tx}}{CLF\cdot IL} \tag{3.36}$$

In these two equations η_{Tx} is the efficiency factor of the transmitting antenna discussed in section 3.4.3.2, P_{av} is the average power received per tuner revolution and P_{max} is the maximum power reading.

3.6.1 Estimation of the Free-space E-Field Radiation

The free space configuration is similar to Paul's description of a far-field free space environment [6], where no ground-plane is placed underneath the EUT and the receiving antenna. The incident waves are the only signal received at the antenna location. So, using the Friis equation method, the OATS E-field equivalent is given by (3.37) for both vertical and horizontal polarisations [6, 36, 38].

$$E_{radiated} = \sqrt{\frac{D \cdot P_{radiated} \cdot 377}{4\pi R^2}} \tag{3.37}$$

where D is the maximum directivity of the EUT.

3.6.1.1 Estimation of the Half-space E-Field Radiation

Sometimes, we perform an OATS measurement under half-space condition. The EUT and the receiving antenna are placed at a specific height above a ground-plane and are separated by a distance S (see figure 3.6). The antenna receives two signals due to the ground-plane reflection: the incident and the reflected wave. To account for the ground-plane effect, a geometrical correction factor named g_{max} is used in the E-field calculation as follows

$$E_{radiated} = g_{max}\sqrt{\frac{D \cdot P_{radiated} \cdot 377}{4\pi R^2}} \tag{3.38}$$

where D represents the maximum directivity of the DUT and g_{max} is given by (3.39) according to the IEC standard [24].

$$g_{max} = \begin{cases} \frac{r}{r_1}e^{-jkr_1} - \frac{r}{r_2}e^{-jkr_2} & Horizontal - polarization \\ \frac{s^2}{r_1^2}\frac{r}{r_1}e^{-jkr_1} - \frac{s^2}{r_2^2}\frac{r}{r_2}e^{-jkr_2} & Vertical - polarization \end{cases} \tag{3.39}$$

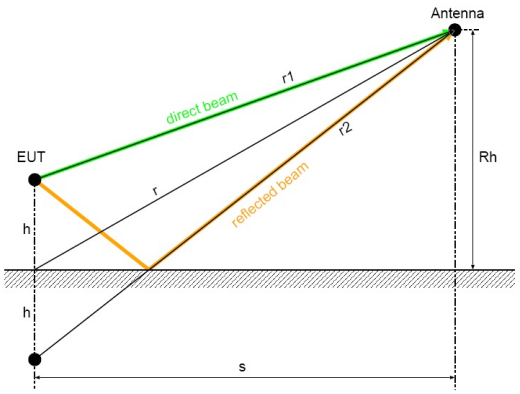

Figure 3.6: Description of the half space OATS configuration [24]

For a typical OATS measurement, where the radiator is placed at 1 m above the ground-plane, g_{max} varies around 6 dB for both polarisations for a frequency above 200 MHz at 10 m away and scanned between 1 m and 4 m [39].

3.7 Metrology Issues

3.7.1 Measurement Correction

A RC application generally involves cables and connectors for signal transport to the transmitting and the receiving antennas. Losses and mismatches are naturally inserted into the setup from the imperfections of these devices. For an effective interpretation of the result, we should correct the transmitted and the received power, P_{input} and $P_{measured}$, according to the following equations

$$P_{Rx} = P_{input} \cdot L_{cableRx} \cdot (1 - |S_{11AntRx}|^2) \cdot AntRx_{eff} \tag{3.40}$$

$$P_{Tx} = \frac{P_{measured}}{L_{cableTx} \cdot (1 - |S_{11AntTx}|^2) \cdot AntTx_{eff}} \tag{3.41}$$

where P_{Rx} is the power received by the receiving antenna, P_{Tx} is the power radiated inside the chamber by the transmitting antenna, $AntRx_{eff}$ and $AntTx_{eff}$ are the antenna efficiencies, finally $L_{cablexRx}$ and $L_{cablexTx}$ are the cables' losses

3.7.2 Averaging

The sequence of data, X, measured from the RC measurement is recorded at different conditions of the chamber due to the stirrer's rotation. Therefore, to calculate correctly the average value of X, we should use the magnitude of each sample in the calculation.

$$if \quad X = (S_1, S_2, ..., S_{N_S}) \quad / \quad S_i \in \mathbb{C}$$

$$\Rightarrow \quad \langle X \rangle = \frac{\sum |S_i|}{N_S} \tag{3.42}$$

3.8 Summary

We have presented and discussed the background concerning the rectangular RC using the waveguide and cavity resonator theories, and the relevant standard for reverberation chamber, IEC 61400-4-21 [24]. We found that modes and stirrers represent the essential features of the RC technique. Some procedures need to be followed to perfectly characterise

the chamber E-field uniformity to achieve an effective measurement. This uniformity investigation consists briefly of three steps which are: the calibration of the chamber, the determination of the field uniformity from the knowledge of the E-field standard deviation, and the uncertainty characterisation of the E-field generated within the working volume of the chamber.

CHAPTER 4

Reverberation Chamber Calibration

In the previous chapter, we examined the RC technique using an analytical approach of the field behaviour inside a region bounded by metallic walls. We simplified the chamber using a cavity resonator model, which is well-known to engineers. As Albert Einstein once said that *"It is certainly true that principles cannot be more securely founded than on experience and consciously clear thinking"*. In this chapter, the principal objective is the application of the IEC calibration to the RC method for the best possible characterisation.

Throughout this chapter, all parameters related to the calibration measurement are analysed. After the computation of the calibration data, we will extend the topic to the validation of the calibration with the OATS E-field equivalent principle.

4.1 Our Reverberation Chamber

The RC of the department, in our radio-frequency laboratory, measures 2.455 m x 3.720 m x 2.475 m in dimension. Two stirrers form the paddling system of the chamber. They were designed by Gideon Wiid in 2005 [37], where four large aluminium sheets of 950 mm x 950 mm are scattered along a carbon fibre axis as shown in figure 4.1.

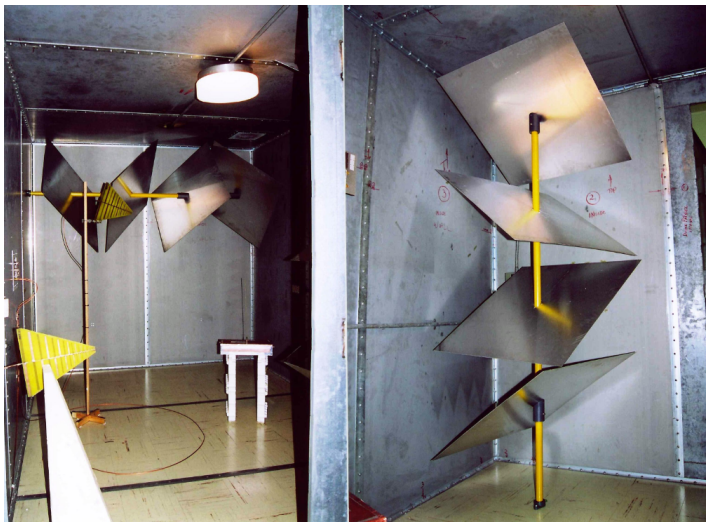

Figure 4.1: The vertical and horizontal stirrers of our department's reverberation chamber

4.2 Preparation for Calibration

4.2.1 Instruments Used and Measurement Precautions

The Vector Network Analyser (VNA) is the preferred instrument for data collection to achieve a quick measurement involving a large frequency range. However, when an external signal generator is used, for instance in the calibration validation in section 4.4, we perform the experiment with a spectrum analyser (SA). Both instruments are switched on an hour before the investigation to have thermal stability and to reduce the drift of the equipment with time [40]. All connectors are cleaned with alcohol and dried with compressed air to eliminate the metallic dust left by previous usage. Furthermore, each connector are tightened with a calibrated torque wrench and the connection is re-checked every time a change was made inside the chamber.

4.2.2 Initial Parameters

The number of samples N_S taken per revolution and per frequency, the frequency range of the investigation and the stirrer's rotation speed constitute the initial parameters of the measurement. No precise formulation is mentioned in the IEC standard [24] concerning the N_S choice. Though, it gives typical N_S values from 100 MHz to 1 GHz (see table 4.1) and recommends a minimum number of 12 for all frequencies of the frequency range. From table 4.1, we adopted a constant value of $N_S = 72$ for all frequencies for three reasons. First of all, we can reach the maximum N_{Ind} that the stirrer can provide by oversampling [31] (see section 3.5). In this way, we also improve the measurement's uncertainty. Secondly, a

large N_S permits one to compensate for the under-moded condition of the chamber at low frequency [24]. Finally, this simplifies the VNA configuration and the measurement's data processing.

Table 4.1: Typical number of samples according to [24]

Frequency range	Number of samples
100 MHz - 300 MHz	50
300 MHz - 400 MHz	20
400 MHz - 600 MHz	16
600 MHz - 1 GHz	12

The calibration is realised under the mode-stirred operation from 300 MHz up to 1.3 GHz to account for the MeerKAT phase-2 frequency band. 300 MHz is particularly employed because it corresponds to the LUF of the chamber according to the work of Wiid in [37].

The stirrer's rotation speed is investigated separately and chosen from three choices of 5 rpm, 8.35 rpm and 30 rpm. The main purpose of this examination is to find the proper speed which gives us the quickest measurement time without altering the data.

4.2.3 Why Stirrer Rotation Speed is Important

In mode-stirred operation, the equipment involved in the measurement, such us the EUT, the probes and the receiver (VNA or SA), are constantly in interaction with the field's variation generated by the tuner rotation. We could measure incorrectly if the receiver cannot follow the field's fluctuation. Obviously, the receiver is able to detect the field's variation with a slow rotation, but the measurement will take more longer. Therefore, we must determine the compromise between the measurement duration, the VNA time-response and the stirrer speed in the first place.

4.2.4 Finding Proper Stirrer Speed

We used two LPDA antennas, placed within the working volume, for the investigation of the stirrer speed from 300 MHz up to 1.3 GHz. The first antenna is fixed and located next to the edge of the working volume, while the second antenna is moved successively in two places. These locations are identified as Position A and Position B in figure 4.2.

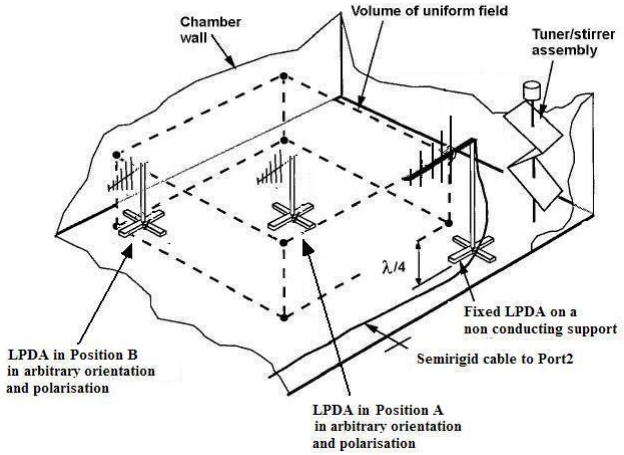

Figure 4.2: Measurement setup for the stirrer speed evaluation, after [24]

Figure 4.3 illustrates the average value of S_{21} with the speeds defined in section 4.2.2 (5 rpm, 8.35 rpm and 30 rpm). These two curves show a deviation of S_{21} within 2 dB from 400 MHz up to 1.3 GHz. A big variation of 8 dB is seen for 300 MHz.

According to table 4.2, two successive samples are delayed by 166.66 ms for the rotation of 5 rpm, 97.22 for the 8.57 rpm and 27.77 for the 30 rpm. These delays are relatively long compared to the time of 4.5 μs that the ZVB needs to measure each sample [41]. This indicates an agreement between the stirrer speeds and the ZVB time-response. Although, the problem we should consider is whether the variations of 2 dB and 8 dB are related to the E-field of the chamber or not.

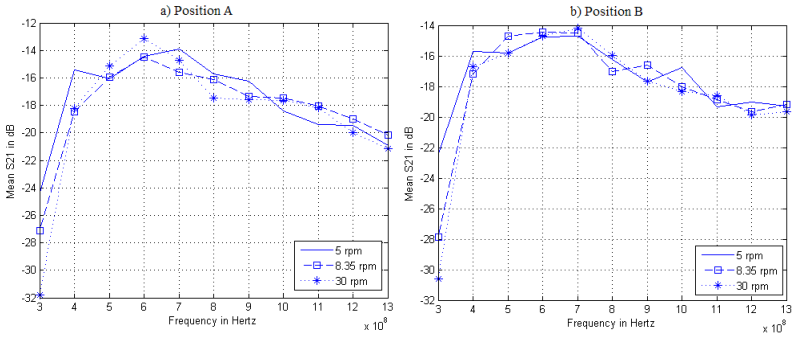

Figure 4.3: Measured S_{21} over one revolution of the stirrer for both speeds. (a) Measured S_{21} in position A. (b) Measured S_{21} in position B

For Bai et al. in [42], the uniformity means: the E-field has the same average, maximum and minimum values inside the working volume. The variation of the mean of the E-field in Position A and Position B plotted in figure 4.4, calculated from (3.27), shows a slight variation of ± 1.8 from 400 MHz up to 1.3 GHz. Accounting for the statistical behaviour

Table 4.2: Time delay between two successive samples for three speeds

Speed in rpm	time in ms
30	27.77
8.57	97.22
5	166.66

of the chamber, this variation is less than the maximum fluctuation tolerable stated in [24]. If we assume that the signal of 300 MHz is less or equal to the LUF of the chamber, a large variation of the E-field is, in this case, expected due to the under-moded status of the chamber for that frequency. As a result, the S_{21} variations we saw in figure 4.3 come from the chamber properties but not from the stirrer's rotation nor the ZVB. Therefore, we used the speed of 30 rpm for further measurements.

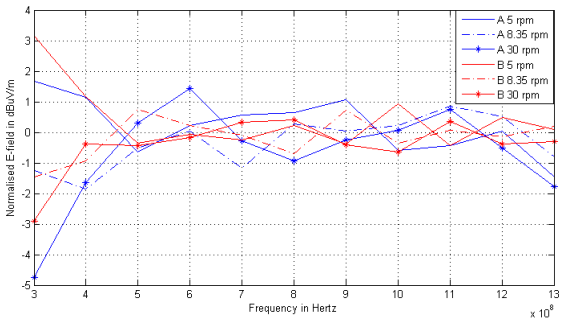

Figure 4.4: Normalised E-field for the three speeds

4.3 Chamber Calibration

4.3.1 Setup Overview

To remind the reader, we calibrated the chamber according to the IEC standard 61000-4-21 using two LPDA antennas placed within the working volume. We positioned the first LPDA at a fixed location, near the edge of the working area, pointing towards the closest corner of the chamber. Thereafter, we successively placed the second LPDA at the eight corners of the calibration. At each location, we carefully orientated the second antenna in a direction not facing the first LPDA to avoid a direct coupling between the antennas. Over the measurement, the VNA (sitting outside of the chamber) and the LPDAs were connected by four better quality coaxial cables. One can visualise the experiment in figure 4.5.

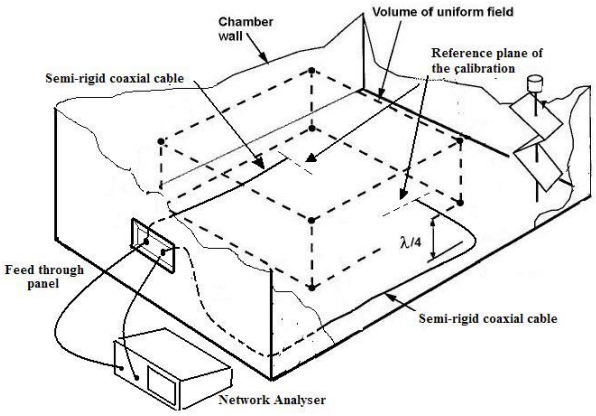

Figure 4.5: Layout of the setup for the calibration of the chamber

4.3.2 Parameters of Interest

For each frequency and at each position of the LPDA, we measured raw data of 72 S-parameters corresponding to the 72 steps of the stirrers. We computed from this data:

- **the attenuations of the chamber**, which are the parameters we need for the calculation of the SE of coaxial cables
- **the E-field generated inside the working volume**, for the uniformity evaluation in section 4.3.3.

To calculate the attenuations, we found first, from the S-parameter, the maximum and the average value of S_{21}. These values are used to compute the maximum and the average power received over one stirrers' revolution using the expression in (3.40). Then, from (3.26), we determined the losses of the chamber. These attenuations are plotted in figure 4.6. We notice here that the calibration measurement is repeatable because the attenuations vary slightly around 0.5 dB over a period of measurement of eight months. We also see from figure 4.6 a smaller attenuation of the signal at low frequency than at high frequency. Additionally, the slopes of the curves look linearly decreasing with the frequency over the frequency range. This behaviour comes generally from the expansion of the electrical length of the chamber with the wavelength of the signal. An extra loss is added each time the frequency increases.

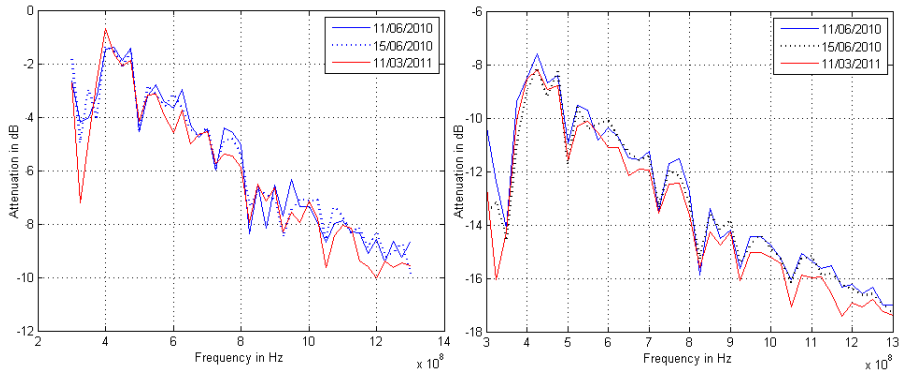

Figure 4.6: The attenuations of the chamber. (a) IL. (b) ACF

Similarly, we also evaluated the mean E-field and the mean of the maximum E-field at the eight corners using (3.27) and (3.28). Figure 4.7 illustrates these E-fields for an input power of 0 dBm. The calculated mean E-field is practically the same, at the eight positions, from 400 MHz to 1.3 GHz (figure 4.7.b). The same behaviour is seen for the maximum E-field curves but with a more bigger variation (see figure 4.7.a). According to the uniformity definition in [42], these results indicate the possibility of field uniformity in the chamber. We can visualise this with the normalised mean E-field plot in figure 4.8.

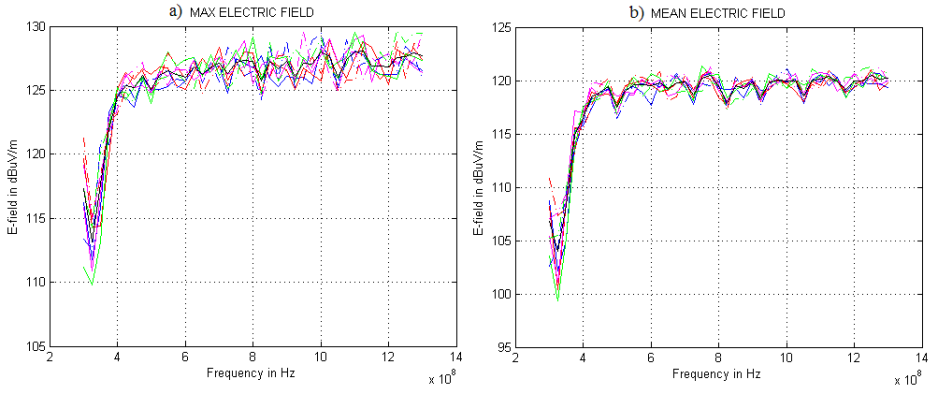

Figure 4.7: The E-field at the eight positions of the calibration. (a) Maximum E-field. (b) Mean E-field

According to the work of Aurand et al. in [43], due to the radiation pattern's shape of a dipole antenna, the LPDA is unable to discriminate between different directions of arrival of the signal. This introduces an error in the calibration measurement. Aurand suggested the usage of a slot antenna (an unidirectional antenna) to consider the effect of the three components of the E-field in the measurement.

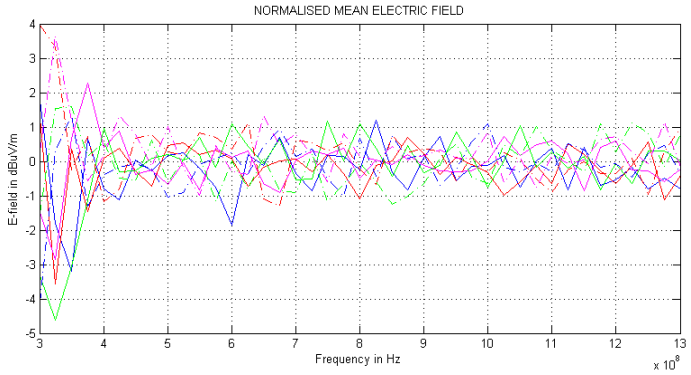

Figure 4.8: Normalised E-field for the chamber calibration

4.3.3 Field Uniformity Evaluation

To examine the quality of the field uniformity of the RC, we have to refer to the acceptable uniformity level outlined in the IEC standard [24]. Briefly, this procedure starts from the evaluation of the E-field generated inside the chamber, which is already covered in section 4.3.2. Afterwards, we calculate the standard deviation of the E-field using (3.30). The reverberation chamber meets the uniformity requirement if the standard deviation does not exceed the IEC uniformity limit.

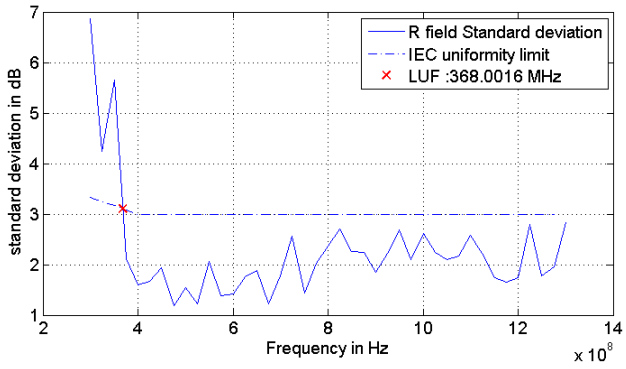

Figure 4.9: Confrontation of the E-field standard deviation to the IEC field uniformity limitation

Figure 4.9 plots the uniformity limitation (the dashed curve) and the standard deviation of the E-field computed from the calibration. We clearly see from this figure that the chamber is in agreement with the IEC requirement from the LUF of 368 MHz up to 1.3 GHz.

4.3.4 E-field Uncertainty Characterisation

In general, the calibration analysis can be terminated after the field uniformity evaluation because we already obtain all the needed parameters for further applications of the facility. These parameters are the attenuations and the LUF of the chamber. The accuracy of the E-field is, however, relevant to prevent the exposure of the EUT to an excess field. This scenario happens particularly for the susceptibility testing. Thus, the uncertainty analysis of the E-field constitutes the completion of the calibration. Moreover, this provides feedback information concerning the number of samples chosen in section 4.2.2 as we will see later in the last paragraph of this section.

The uncertainty analysis began with the evaluation of the number of independent samples among the 72 samples we collected per stirrers' revolution. With the autocorrelation function in (3.31) we calculated the correlation coefficients of the data for ten frequencies (see figure 4.10). Thereafter, with the offset Δ of each curve, when the curve intersects the *IEC correlation limit of 0.37 (1/e)*, we computed the number of independent samples N_{Ind} (in table 4.3) using (3.32). Finally, since the measurement with the LPDA antenna responds to one dimension of the field only, we evaluated the confidence interval of the E-field using (3.33) with z equal to 1. The results of these computations are summarised in table 4.3.

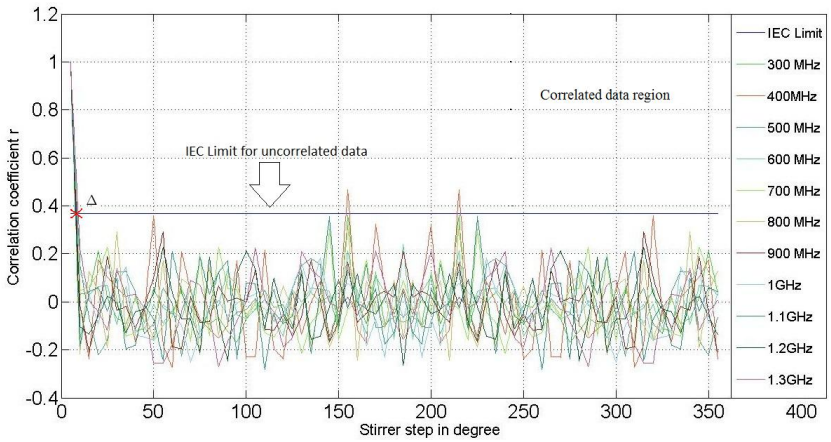

Figure 4.10: Correlation coefficient of the 72 samples versus the tuner position in degree. The correlation limit of 1/e proposed by the IEC standard is represented by the horizontal line

The accuracy of the confidence interval, presented in table 4.3, depends entirely on the accuracy of N_{ind} if we refer to the expression in (3.33). With the autocorrelation function, we could not determine N_{ind} precisely because the correlation coefficient itself is a random variable with its own uncertainty associated with its distribution [34]. Consequently, the uncertainty on N_{ind} adds to the field's statistics uncertainty and the measurement

uncertainty [44]. This gives rise to an expanded uncertainty.

The threshold of 0.37, which is the appropriate correlation limit for infinite samples, is also questionable due to the statistical nature of the correlation coefficient [24]. The discussion concerning the evaluation of N_{Ind} in [24, 33, 34, 45] shows that the critical value of the correlation changes with N_S and it is less than 0.37 for a finite N_S. For $N_S > 100$, the IEC standard [24] evaluated the expression of the threshold from curve fitting as follows

$$r \approx 0.37\left(1 - \frac{7,22}{N_S^{0,64}}\right) \tag{4.1}$$

But, (4.1) was not applied since a lower number of samples was taken. Therefore, the values of N_{Ind} in table 4.3 are overestimated. Yet, this tables gives an overview of the field's statistics of the chamber.

Table 4.3: Number of independent samples and the E-field 95% confidence interval

Frequency in MHz	N_{ind}	95% Confidence interval in dB
LUF	41.574	2.7265
400	47.597	2.5374
500	47.5	2.5402
600	43.11	2.6743
700	44.731	2.6223
800	46.271	2.5757
900	42.823	2.6838
1000	45.994	2.5839
1100	47.884	2.5294
1200	46.349	2.5734
1300	41.86	2.7165

According to the expression in (3.33), once we reach the maximum N_{Ind} that the stirrer can provide, increasing N_S does not improve the E-field uncertainty level. Thus, we can reduce the number of samples to a certain limit (around 50) to shorten test cycles. However, in this case, the chamber would need to be re-calibrated to update all the chamber's parameters.

4.4 Calibration Validation

4.4.1 Method

Different method exists for the validation of an experimental results. One compares the measurement to computational or analytical models. Another uses published data as a reference. Concerning the chamber calibration, testing the chamber with something already known, such as the OATS E-field estimation of a reference radiator, seems the simplest way.

4.4.2 The Standard Radiator

The emissions reference source (ERS) used for this investigation was manufactured by Laplace Instruments. It was calibrated by the National Physical Laboratory (NPL) using the following half-space OATS configuration:

- Measurement location (from the ERS): 3 m
- Antenna scanned height: 1 m to 4 m
- Frequency range: 30 MHz - 1 GHz
- Frequency step: 2 MHz
- Polarisation: horizontal and vertical

4.4.3 Measurement Description

The measurement is based on the evaluation of the total power radiated by the ERS inside the chamber. A SA collects data from the LPDA antenna located at the edge of the working volume, as shown in figure 4.12.c. For best results, we configured the experiment according to the calibration configurations as follows:

- A polystyrene block is used to support the radiator within the working volume.
- The LPDA antenna is placed at the same location as its position during the calibration.
- The sweep-time of the SA is set equal to 27 ms to obtain 72 samples per revolution.

4.4.4 ERS Loading Factor

It is important to notice that the same polystyrene block was used to support the LPDA at the eight corners of the working volume during the calibration of the empty chamber. So, its effect is already included in the calibration data. Hence, the loading factor of the chamber would be equal to 1 due the smallness of the ERS compared to the RC volume. Nevertheless, we checked the radiator effect on the chamber using the procedure in section 3.4.4. The calculated CLF is plotted in figure 4.11. Obviously, it confirms the hypothesis.

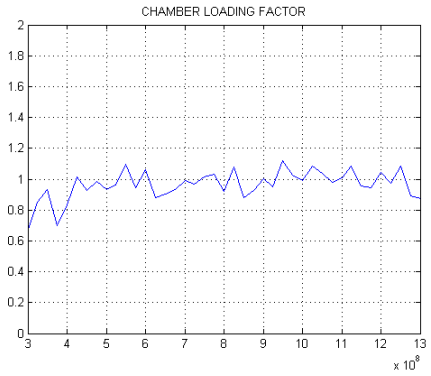

Figure 4.11: The standard radiator loading factor

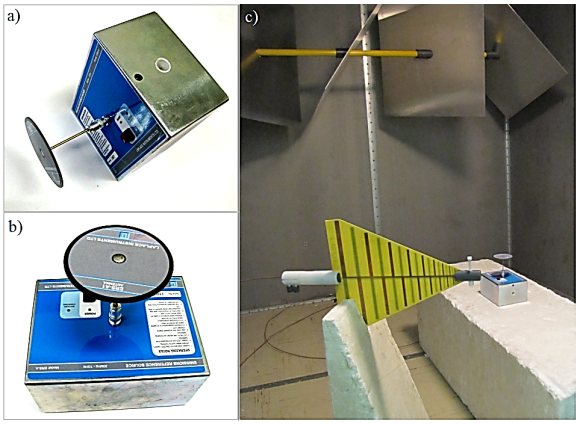

Figure 4.12: Setup for the estimation of the OATS E-field equivalent. a) Horizontally Polarised radiator. b) Vertically polarised radiator. c) Description of the setup showing the receiving LPDA antenna and the standard radiator above a polystyrene foam

4.4.5 Finding the Proper Orientation of a DUT

The first question we must consider when we perform the Z_T experiment is the orientation of the CUT within the working volume. The isotropy of the signal inside an ideal RC, seen

in section 3.3.2.3, means that the DUT orientation should not influence the measurement. However, it is worth checking the accuracy of this property for a real chamber.

We oriented the ERS in three directions (figure 4.12) and measured the power radiated by the device for each polarisation. These orientations corresponded to a vertical polarisation and two orthogonal horizontal polarisations named X axis and Y axis in figure 4.13. Almost the same power is received from the device, according to figure 4.13.a, within a difference of 2 dB (see figure 4.13.b). Accounting for the statistical behaviour of the chamber, which introduces a variation in the S-parameter data (similar to the S_{21} curves in figure 4.3), we believe the differences in figure 4.13.b is independent of the orientation of the ERS. Therefore, we can orientate the CUT in any direction for the Z_T investigation.

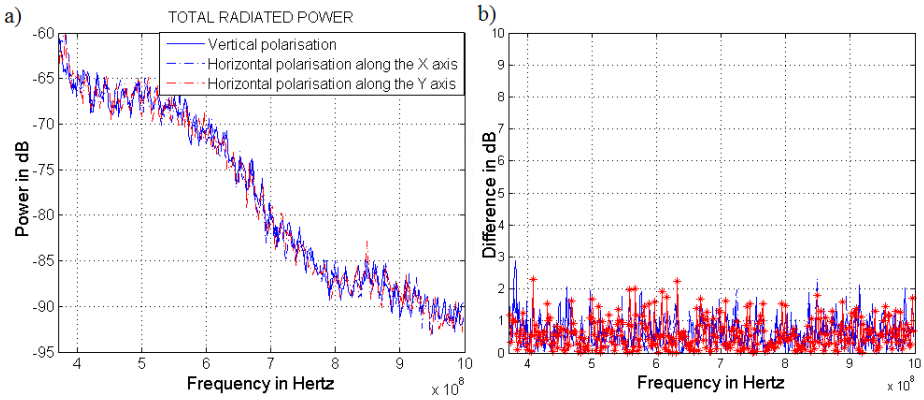

Figure 4.13: The measured total radiated power for both polarisation (a) and the normalised power variation (b)

4.4.6 OATS E-field Equivalent Estimation

The OATS E-field equivalents, calculated from the power measurements using (3.38), are shown in figure 4.14 for the horizontal and vertical polarisations. The calibration curves of the radiator, provided by NPL, are also displayed in these figures for visual comparison with the two estimated OATS E-fields.

For both polarisations, the correlation between the measurement and the calibration data are quite good, within 5 dB, from the LUF of the chamber up to 700 MHz. Then, it becomes worse beyond 700 MHz. This behaviour could be due to the drift of the ERS since the last calibration of the device was made in October 2007. Thus, we repeated the same measurement using a newly acquired ERS, calibrated by NPL in February 2010, to recheck the correlation. The results of the new measurement are plotted in figure 4.15. Apparently, the correlation is better for all the frequencies of the frequency range. However, for an accurate appreciation of the OATS E-field results, it is suitable to realise an OATS E-field

measurement of the radiator.

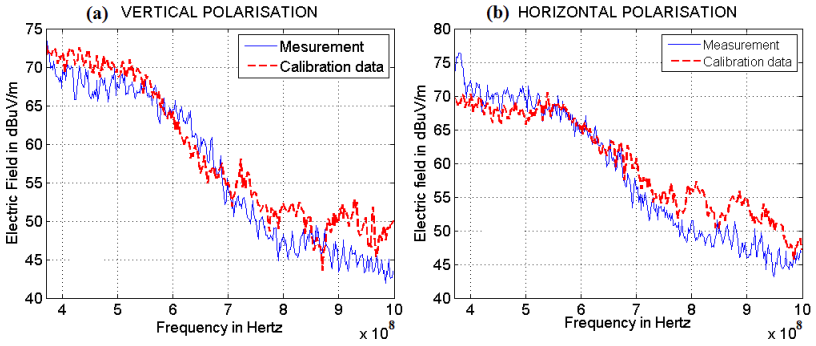

Figure 4.14: Estimated OATS E-field equivalent for the old standard radiator calibrated in October 2007. a) For the vertical polarisation. b) For the Horizontal polarisation

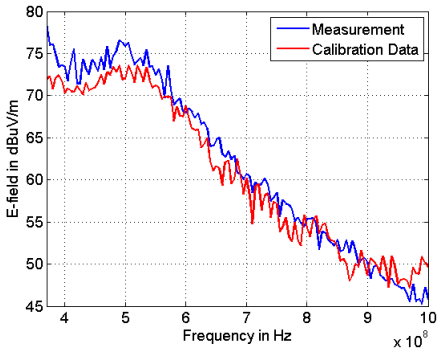

Figure 4.15: Estimated OATS E-field equivalent for the new standard radiator calibrated in February 2010. a) For the vertical polarisation. b) For the Horizontal polarisation

4.5 Summary

This chapter presented the calibration of our RC according to the IEC 61000-4-21 standard. Here, the spotlight was on three basic ideas:

- Which stirrer speed is better for the calibration?
- How good is the calibration?
- What should be the best orientation of the DUT placed within the working volume of the chamber?

The OATS E-field estimation principle was used to validate the chamber measurement. This provided a good correlation to the OATS E-field data of a well-known reference radiator. However, an OATS E-field measurement of the radiator should be undertaken for better appreciation of the results.

CHAPTER 5

Wideband Coaxial Cable Transfer Impedance Investigation

SHIELDING evaluation and design constitute one of the important fields in EMC for RFI mitigation. Often, the EM emissions produced by nearby equipment induces cable currents and voltages which are comparable to the useful signal of an electronic system. For coaxial cables, the external conductor is specially manufactured to protect the current leakage into the internal region. However, coaxial cables are imperfect as seen in chapter 2. Braided or made of homogeneous cylindrical tube, coaxial cables' shields are efficient for a limited frequency range. After the theoretical analysis of noise penetration through the shield, which provided the fundamentals of coaxial cable shielding, we will focus here plainly on the practical examination of coaxial cables shielding. The reverberation chamber and the current injection techniques will be combined to achieve this objective. A coaxial air-line and some coaxial cables samples identified on the KAT-7 dishes will be used to illustrate the methodology application.

5.1 Methodology Refinement

The difference between the LUF of the chamber, found in section 4.3.3, and the resonant frequency of the field to wire method, in section 2.6.3.2, leads to incomplete Z_T data in the region not covered by the methodology. This is situated approximately between 75 MHz and 370 MHz. Due to the linearity of Z_T at high frequency (see section 2.5.2.5), we

can use a linear interpolation to compute the unknown Z_T data.

Thus, in summary (see figure 5.1), we investigate the two parts of the Z_T separately with the two methods. Then, these parts are combined and interpolated to determine the full Z_T. Afterwards, we plot the Z_T of all the cables involved in the measurement in the same figure for classification.

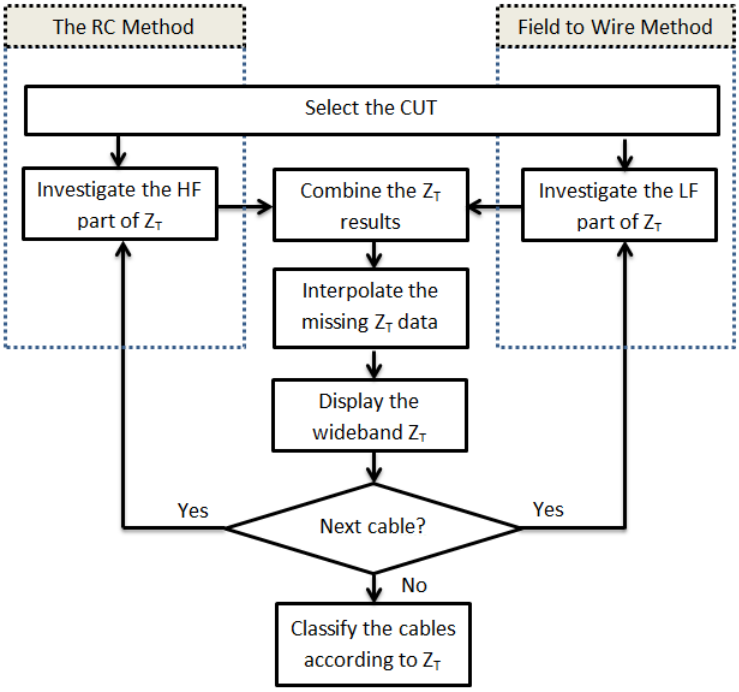

Figure 5.1: Refined wideband coaxial cable Z_T methodology flowchart

Before proceeding, let us review the important keys of the two methods.

5.2 Measurements Specifications

5.2.1 Low Frequency Setup

For the low frequency investigation in figure 5.1, the CUT is matched to a 50 Ω load at both ends. The CM current generated by the EM injection clamp over the external conductor is measured through the CP sitting at the left-hand side of the setup (see figure 5.2.b). A three-port VNA is used to measure, simultaneously, the CM current and the DM voltage induced across the centre conductor of the CUT. Port 1 generates the excitation signal of the whole setup. Port 2 measures the DM voltage induced on the cable. Port 3 drives the CP. This configuration permits a quicker measurement. The same

measurement could be performed with a two-port VNA. The CM current and the DM voltage are measured one by one in this case.

Figure 5.2: The setups for the wideband Z_T measurement: a) the reverberation chamber for the SE measurement, b) setup for the current injection

The lowest frequency is 300 kHz due to the characteristics of the available VNA while the highest limit depends upon the cable's length.

5.2.2 High Frequency Setup

The CUT is also matched for the high frequency measurement in figure 5.2.a. It is placed within the working volume of the chamber on a polystyrene block. A signal of known power (from 300 MHz to 1.3 GHz) is injected into the chamber, through the LPDA antenna seen on the right-hand side of the CUT, to account for the MeerKAT phase-2 frequency range. From this measurement is calculated the SE of the CUT using (2.19). Afterwards, the Z_T of the cable is computed from the expression in (2.20).

According to the discussion in section 4.4.4 concerning the loading effect of the ERS, the CUT would also have a negligible effect on the chamber. Thus, the loading factor of the setup is assumed equal to one.

5.3 Preliminary Tests

5.3.1 SE Measurement Connectors Effect

For the SE investigation, the connectors used at the ends of the CUT take part in the measurement if the matched CUT is placed within the working volume (see figure 5.2.a).

The connectors and the CUT are exposed to the same signal over the measurement. The imperfection of the contacts, between the connectors and the CUT, introduces small gaps in the setup which increases the EM coupling at high frequency. The connectors' SE evaluation is beyond the scope of this chapter. However, it can be checked using the setup in figure 5.5 where the CUT is removed and replaced by a matched configuration of SMA and N-type connectors.

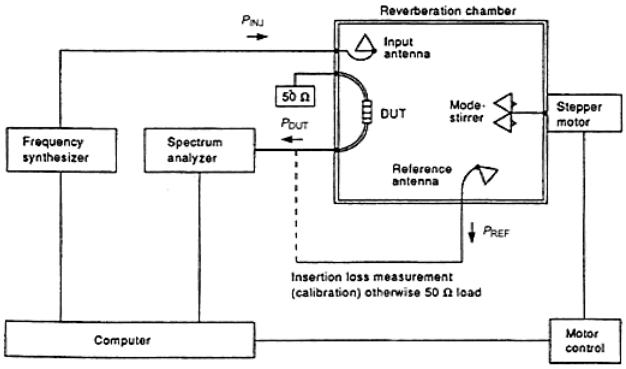

Figure 5.3: The correct CUT SE measurement setup according to the standard [25]

The proper cable arrangement for the SE measurement which removes the connectors' coupling, as recommended by the IEC standard in [25], is the one shown in figure 5.3. Indeed, connecting the CUT at the interface panel of the wall and placing the matched load outside of the chamber will reduce the number of connectors involved in the measurement. Nevertheless, the difficulties of this setup remain on the cable configuration. One should remember that the CUT should not exist outside of the working volume region. The distance between the wall and the CUT must be bigger than the wavelength corresponding to the LUF of the chamber, otherwise the CUT will experience a non-uniform field area situated near the walls. To solve this issue, Démoulin and Koné used a good shielded cable, more than two times the wavelength of the LUF, to extend and support the CUT inside the working volume (see figure 5.4).

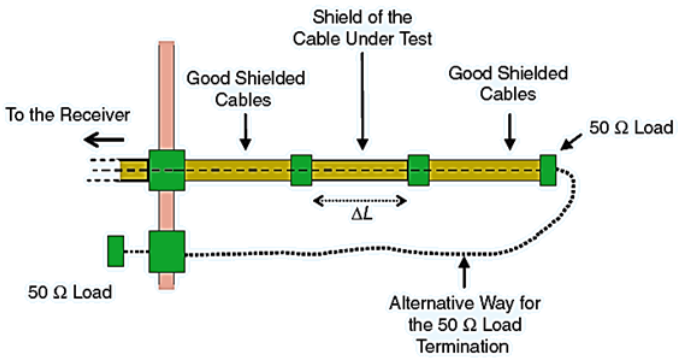

Figure 5.4: Variant setup of the cable SE measurement by Démoulin and Koné [46]

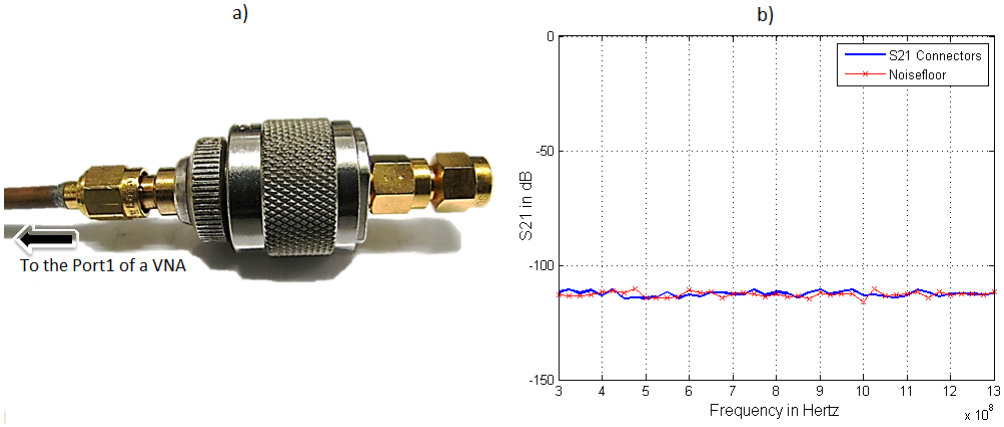

Figure 5.5: Evaluation of the connectors' effect: a) the connectors configuration placed above a polystyrene block and illuminated by the uniform EM signal inside the working volume of the chamber, b) comparison between the measured S_{21} and the system noise-floor

However, attention must be given to the connection between the piece of good shielded cable and the CUT. Moreover, the non-flexibility of some cables, particularly a coaxial air-line, requires an alternative way to connect the 50 Ω load, placed outside of the chamber, to the other side of the CUT. The preferred setup seems too costly for us and the use of connectors is unavoidable. To alleviate this situation, we checked the connectors' effect first over our frequency range. If it is noticeable, conductive tape will be used to isolate the connectors. We note that Démoulin and Koné used this setup for a frequency range of 1 GHz to 7 GHz.

We replaced the CUT in figure 5.2.a by the configuration in figure 5.5.a to detect the EM coupling through the connectors. The new setup was illuminated by the signal from the LPDA over the measurement and the S_{21} recorded by the VNA is represented in figure 5.5.b by the curve in blue. The noise floor of the setup was also measured when the LPDA and the connectors under test were disconnected. The comparison between the noise-floor and the S_{21} shows no major difference over the frequency range of the investigation. It means the connectors can be left exposed to the radiated signal during the SE measurement.

5.3.2 CUT Current Distribution

If we refer to the Z_T definition in figure 2.6, the current's distribution over the braid of the CUT has a direct impact on the Z_T investigation. A uniform current distribution is necessary, over the cross-section and the length of the cable, for better measurement. In this instance, all the imperfections of the cables contribute equally in the coupling process.

For the reverberation chamber method, the presence of relative field uniformity within the working volume creates a uniform current distribution across the braid for any length of cable. This is the principal reason why the SE measurement does not depend on the length of the cable. However, for the field to wire method, we can identify two potential sources of Z_T measurement variation:

- Firstly, the CUT is approximately placed at the centre of the CP during the experiment. This might introduce a slight variation on the CM current reading between successive measurements.
- Secondly, the setup shows a resonance due to the electrical length of the CUT. A standing wave appears over the braid at high frequency. As a result, the CM current reading might be different at different positions of the clamps (the EM injection clamp and the CP).

Three measurements of the CM current have been performed for three positions of the CP, PosA to PosC as shown in figure 5.6, to check the effect of the CP location on Z_T. A minimum distance of 25 cm is set between PosC and the EM injection clamp to prevent the coupling between the two devices as mentioned in [5]. The results of the measurements are shown in figure 5.7 for the coaxial air-line described in figure 5.9.

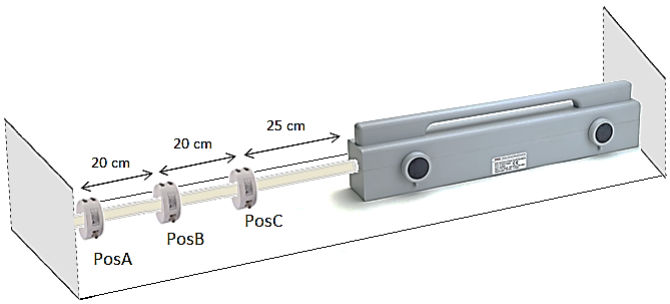

Figure 5.6: Checking the effect if the CP position

The resonance of the cable becomes more visible when the wavelength of the signal is more than four times the length of the CUT. It starts from 57 MHz for the cable we used in this investigation. In figure 5.7.a, we clearly see the divergence of the CM current at the three positions from 20 MHz up to the resonance frequency limit of the CUT. This variation leads to a change in the Z_T of the cable but, as we can see from figure 5.7.b, the difference between the three Z_T is small. So, as far as the resonance condition of the setup is concerned, the CP location is not significant for Z_T. We adopted the CP in PosA for the Z_T evaluations.

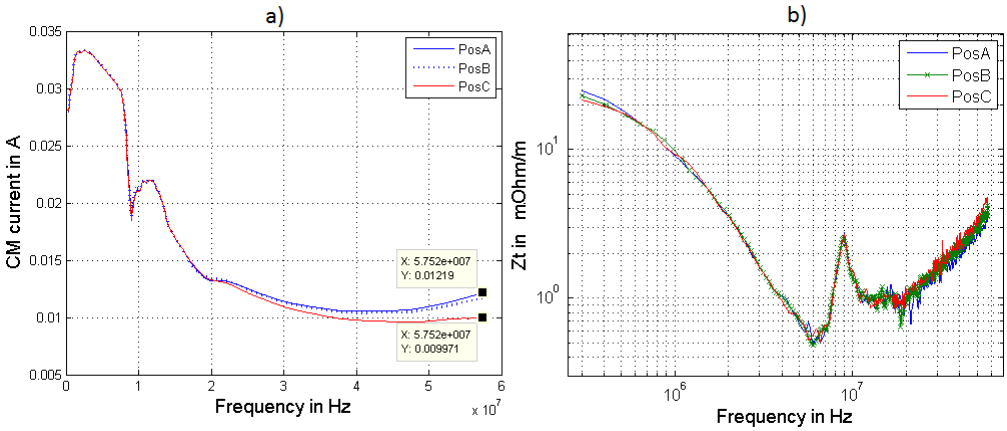

Figure 5.7: The CM current variation with the CP position: (a) the CM current at the three positions, (b) the corresponding Z_T variation

Similarly, the orientation of the injection clamp is checked for two configurations (setup1 and setup2) while the CP remained in PosA. For Setup1, the input of the device is located at the left-hand side of the injection clamp in figure 5.6. For Setup2, the clamp is rotated by 180° from its previous position. The results of the measurements are displayed on figure 5.8.

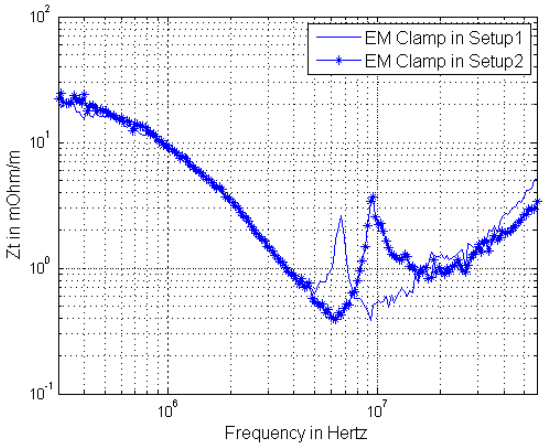

Figure 5.8: Variation of Z_T regarding the orientation of the EM injection clamp

Here, the measured Z_T is the same except around the peaks. These resonances were identified as coming from the loop between the VNA, the current injection circuit (formed by the cable in port1 and the EM injection clamp) and the DM voltage measurement circuit (formed by the cable from Port2 to the CUT). These resonances were minimal, even unnoticeable, for a CUT of small diameter (approximately less than 4 mm). The loading effect of the coaxial air-line, which is 8 mm in diameter, on the EM injection clamp appears to be the origin of these peaks which changes the internal characteristics of the

EM injection clamp.

A better measurement policy would have been to take all cables through the L-plate barrier. This, however, complicates the physical setup. Its main consequence is that the resonance would then be removed. This does not change the findings.

5.4 Methodology Validation

A major issue we found in the cable Z_T investigation is the lack of coaxial cables' Z_T data for the validation of the measurement. The Z_T of some generic cables such as an RG58 and an RG174 are available, but only for limited frequency bands.

A coaxial air-line seems a promising means to compensate the database limitation for the validation of the measurement. It corresponds adequately to the Vance model described in section 2.5.2.3.

5.4.1 Coaxial Air-line Wideband Z_T Characterisation

5.4.1.1 Air-line Geometry

A sketch of the coaxial cable is shown in figure 5.9. It is made of a cylindrical tube, in brass, of 1.3 m length with a single circular hole on the shield. Two N-type female connectors terminate the model at both ends of the cable.

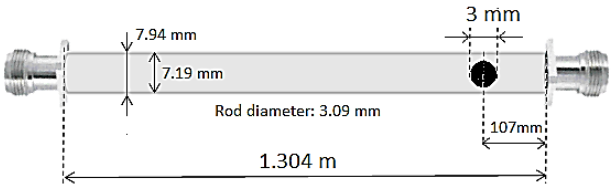

Figure 5.9: Geometry of the coaxial air-line

5.4.1.2 Z_T at Low Frequency

For the low frequencies part, we placed the perforated region of the model at the CP side. If the hole is kept inside the EM injection clamp, the direct illumination of the hole will distort the measurement's response. Apart the peak at 9 MHz in figure 5.10, good correlation is seen between the Vance model and the Z_T computed from the measurement using (2.23).

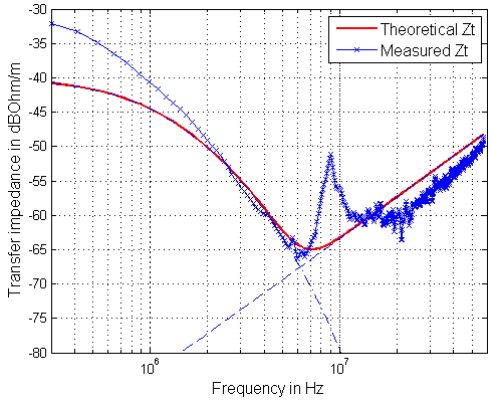

Figure 5.10: Z_T of the coaxial air-line at low frequency

5.4.1.3 Z_T at High Frequency

For the reverberation chamber method, two configurations have been considered as shown in figure 5.11.a. The hole is close to port 1 for the measurement in config 1. Conversely, it is close to the 50 Ω load for config 2. The results of the measurements are plotted in figure 5.11.b.

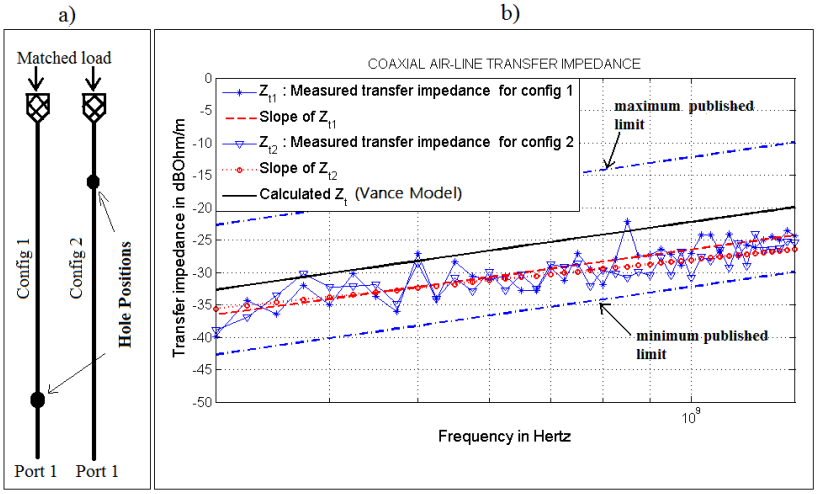

Figure 5.11: (a) Description of the measurement for the high frequency part of the air-line Z_T. (b) Comparison between the Vance Model, the measurements and published Z_T data

According to Hoeft [22], measurement and polarizability theory agree within ±10 dB (dashed blue curves of figure 5.11.b). In our case, we found that the theoretical Z_T (given by the model of Vance) and the measurements (averaged Z_T in red) agree within 4 dB across the frequency range.

Both of the two averaged Z_T also show the slope of the variation of the two measured Z_T. For config 1 (dashed red curve of figure 5.11.b), the theoretical variation of 20 dB/decade

is verified. For config 2, the hole is located further from Port 1 than its location in config 1. So, the resistance effect of the centre conductor attenuates the signal, especially at high frequency, and causes a reduction of the Z_T slope for that configuration. We conclude from these results that:

- the air-line model agrees with Vance's Z_T model,
- an acceptable Z_T measurement of coaxial cable can be achieved with the reverberation chamber. This last point can also be interpreted as a validation of the chamber calibration.

5.4.1.4 Wideband Z_T

Figure 5.12 presents the wideband transfer impedance of the coaxial air-line. Again, the high frequency parts of the two Z_T, from the low and the high frequency measurements, were linearised and interpolated to see the Z_T variation over the frequency range. An interesting point we found from this plot is the linear correlation between the low and high frequency parts of Z_T (the red line of figure 5.12), i.e. the agreement between the field to wire and the RC methods. This verifies quite convincingly Vance's Z_T variation of 20 dB/decade.

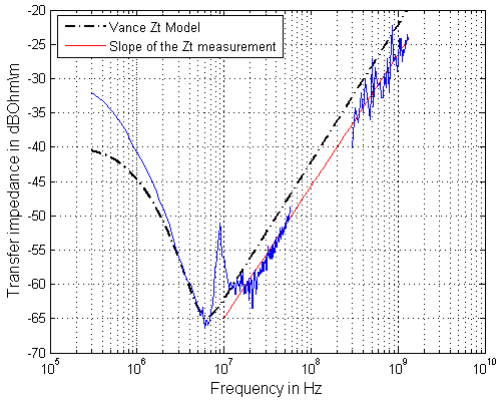

Figure 5.12: Comparison between the air-line theoretical Z_T and measurement

5.4.2 RG58 and RG174 Wideband Z_T Characterisation

The next step of the validation concerns the evaluation of the quality of the Z_T results for braided cables. In brief, the Z_T of a braided cable has a third component coming from the braiding characteristic of the cable. The other two coupling components remain present.

In [47], Fourie et al. studied the Z_T variation of two RG58 cables from different manufacturers. Accounting for literature-published Z_T values of an RG58, they found a Z_T difference within 10 dB across a frequency range of 10 MHz to 500 MHz. We measured the Z_T of the same coaxial cable using the methodology presented in figure 5.1. In figure 5.13, the result of the computation is plotted and compared to Fourie's results which are represented by the triangles. This shows that the calculated Z_T lie well within Fourie's Z_T variation.

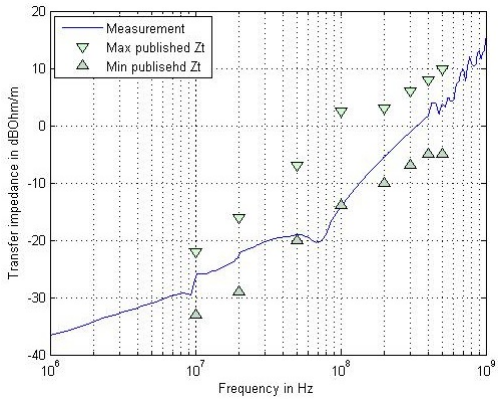

Figure 5.13: Comparison of our results with Fourie's RG58 Z_T

Considering the work of Moriello and Benson in [17, 5], using the current injection technique. We firstly see a similar pattern trend between our RG58 and RG174 Z_T and their results (figure 5.14). Secondly, a difference of 5 dB is seen across the frequency band. Benson also noticed in their work [5] that an order of magnitude variation is often obtained on coaxial cables coming from different manufacturers. Taking into account Benson and Fourie findings, the observations in figure 5.14 are a characteristic of the particular cable we have from our suppliers. We can conclude that the methodology is providing realistic data for braided coaxial cable Z_T.

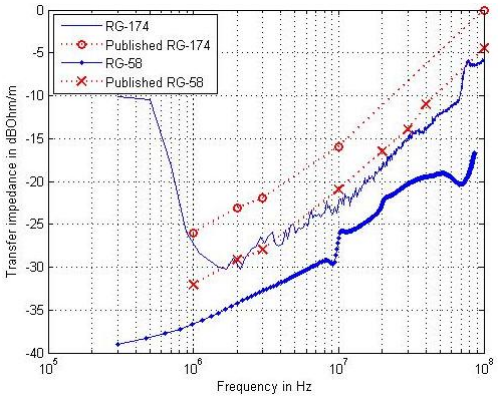

Figure 5.14: Comparison between Moriello's Z_T and our results for an RG58 and an RG174

5.5 SKA Coaxial Cables Classification

Some samples of coaxial cables, identified on the KAT-7 dishes, have been measured using the methodology. Four cables are shown in figure 5.15 to illustrate the classification of coaxial cables using Z_T. These cables are an RG58, an RG174, a B-60 from Huber and Suhner and a Multiflex 141 from Suhner.

At first, this figure confirms the correlation between the field to wire method and the RC results. The best cable has the lowest Z_T value. We also observed a similar trend between the four curves at high frequency. A careful examination of the Z_T of the RG cables shows that a slope variation occurs around 100 MHz. These slopes are represented by the two dashed lines. This behaviour does not conform to the Vance Z_T model. To discuss this slope variation, in the next section, we reviewed Tini's improvement on Vance's model and its effect on Z_T.

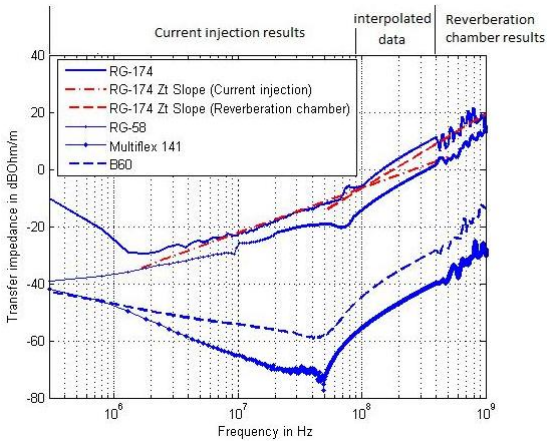

Figure 5.15: The wideband Z_T of four KAT-7 coaxial cables

5.6 Tini's Braided Cable Model Verification

Tini's braided coaxial cable model introduces an additional coupling term in Z_T to consider the porpoising effect of the braid. Referring to the Tini and Demoulin observations described in section 2.5.2.5, the new coupling term varies with $\sqrt{F}$. Analytically, the equation in (2.14) can be rewritten as follows at high frequency.

$$Z_T \approx j\omega L_H \pm j\sqrt{\omega} L_B \tag{5.1}$$

where L_H represents the holes' inductance and L_B is the porpoising inductance.

Following Tini's new formulation of Z_T, ω brings a 20 dB/decade variation at high frequency while $\sqrt{\omega}$ introduces a 10 dB/decade variation. For a lower frequency range, the difference between these two variations is not considerable. Thus, the combined Z_T slope is less than Vance's prediction of 20 dB/decade. For a higher frequency band, the $\sqrt{\omega}$ values are smaller and end up being negligible compared to ω, i.e. the holes' coupling finishes by dominating Z_T. In this case, Z_T tends to the Vance 20 dB/decade variation. This slope behaviour of Z_T is seen in figure 5.15 for the RG58 and the RG174 cables. Between 1 MHz and 10 MHz, we have a variation less than 20 dB/decade while from 10 MHz it increases. This was also noticed by Hoeft, in [48], concerning his work on shielding performance of commonly used braided cables. We believe, this slope variation corresponds to Tini's model behaviour described above. However, there may also be a more complex phenomenon occurring with these cables.

5.7 Methodology Limitation

The success of the methodology depends closely on the quality of the CUT and the dynamic range of the VNA. For good shielded cables, the S_{21} of the field to wire method is near the noise-floor for some frequencies. This increases the uncertainty of the measurement at those frequencies. At the same time (see figure 5.15), the Z_T curves of these cables are not particularly informative concerning the holes and braids coupling, because the curves are dominated by the wave diffusion through the cables' shield. Few data are available for the interpolation process. Consequently, we cannot trust the slope given in the region not covered by the methodology. For example, the slope of the multiflex 141 and the B60 between 70 MHz to 400 MHz, in figure 5.15, could be less than the slope shown in this figure, but it should not also exceed the maximum variation of 20 dB/decade. In this case, the interpolation gives us the worst case of the variation, not necessarily the proper values of the Z_T in this region.

Accounting for the length of the EM injection clamp (60 cm) and the recommended distance of 25 cm between the two clamps of the current injection method, the lowest CUT we can use is 85 cm. This corresponds to a maximum resonant frequency of 88.2 MHz. With Benson's setup, using a CP for the current injection, we can reduce the length of the CUT to 25 cm and extend the frequency range up to 300 MHz. This allows us to improve the interpolation issue, stated previously, as long as an amplifier is used to increase the CM current level.

5.8 Recommended Z_T Methodology for MeerKAT

For the MeerKAT and SKA project, the reverberation chamber has a large advantage compared to the field to wire technique if we consider all the EMC testing we can perform with such a facility. For the Z_T measurement in particular, we used the field to wire method because our chamber is limited to the LUF of 370 MHz. With a more bigger room, characterized by a LUF of 300 kHz, the reverberation chamber technique is adequate for the characterisation of the wideband Z_T. Moreover, extending the investigation beyond 1.3 GHz is possible, but the connectors' effect should be taken into account.

The reverberation chamber method is rather better for laboratory measurement than in-field measurement. Due to its portability and its adaptability with the cable length, the field to wire method is more convenient for quick investigation and verification of cables in use on the telescopes site. Also, the CUT is intact after the measurement.

The methodology can be reduced to the field to wire method alone for the in-field investigation. For this situation, only the diffusion effect of the cable is measured, the high frequency part of Z_T is approximated with Vance's model of 20 dB/decade. Clearly, the procedure is not accurate, especially for a cable with an optimised braid. However, it permits a quick and global visualisation of the cable status.

5.9 Summary

The application of the wideband Z_T methodology was presented in this chapter for coaxial cable classification. An interpolation was used to estimate the unknown Z_T in the uncovered region by the methodology. The following facts have been noticed:

- The field to wire and the RC Z_T were in agreement
- The coaxial air-line confirmed the theoretical variation of 20 dB/decade. The measurement concurred with the polarizability theory within 4 dB
- Tini's porpoising effect was noticed on two braided coaxial cables. The Z_T started with a smaller slope at low frequency before reaching the 20 dB/decade variation.

We also found that the methodology cannot give an accurate result for good shielded cables due to the resonance of the field to wire method. Finally, some recommendations were presented for the application of the methodology on MeerKAT.

CHAPTER 6

Conclusion, Recommendations and Further Work

6.1 Conclusion and Recommendations

The examination of coaxial cables' screening effectiveness is presented in this thesis using Z_T and SE concepts. This illustrates the process of coaxial cable classification for RFI mitigation for the cabling of an electronic system. Accounting for the sensitivity of KAT-7 and MeerKAT, such an examination is relevant for the success of the project because coaxial cables are sometimes the connection to the world surrounding the system. Regardless of the nature of this connection, a deliberate contact between equipment, or one coming from capacitive linkage, the presence of CM mode current over the external conductor of coaxial cables is unavoidable. The Z_T was evaluated over a frequency range of 300 kHz up to 1.3 GHz. The reverberation chamber technique and a field to wire method have been combined to determine the Z_T over such a large frequency range.

Discussion concerning the fundamentals of coaxial cable shielding analysis was presented in chapter 2. Here, we tried to find the analytical model which governed the EM coupling mechanism on coaxial cables. The noise penetration through tubular homogeneous shielded and braided coaxial cables was particularly studied. Two major formulations have been reviewed: the coaxial cable model of Vance and of Tini. In both cases, Z_T decreases with F at low frequency. The magnetic coupling through holes and from the braid porpoising take over the diffusion part at high frequency with a slope of 20 dB/decade for Vance's

model. A slope of 10 dB/decade is introduced by Tini's porpoising inductance. This chapter also focused on the wideband Z_T methodology identification.

After this literature survey, the reverberation chamber technique was detailed using waveguide and cavity theory. The IEC standard 61000-4-21 calibration principle was particularly analysed for the calibration of our reverberation chamber. Thereafter, we calibrated the chamber and the measurement results were discussed in chapter 4. This investigation showed us a normalised mean E-field variation within ± 1.2 dB. The chamber conformed to the IEC uniformity requirement from 370 MHz.

The next step of the study concerned the chamber's calibration validation. Since no additional data was available, such as simulated results, we decided to use the OATS E-field equivalent estimation for the validation. This experiment involved two well-known standard radiators calibrated by NPL in 2007 and 2010. Good correlation within 4 dB was found between the estimated OATS E-field and the calibration data of the radiator. However, an independent OATS E-field investigation of the radiator is recommended for a more precise appreciation of the chamber calibration. For example, we found that there are loading effects of the standard radiator in the chamber. By inserting a 10 dB attenuator pad this loading would be minimised. The radiator should then be checked on a calibrated OATS with the 10 dB pad included. So far, the mode-stirred operation is the only technique used for the calibration measurements. We believe that a re-calibration of the chamber using another mode, such as a mode-tuned technique, is also interesting for the validation of the chamber's calibration. This would allow the comparison of both calibrations.

The last part of the thesis concerned about the wideband Z_T determination of KAT-7 coaxial cables samples. A coaxial air-line was specially built for the validation of the methodology which was refined due to the frequency band limitation of the reverberation chamber and the field to wire method. Three important results have been found:

- Firstly, the field to wire and the RC Z_T results were correlated.
- We verified the 20 dB/decade variation stated by Vance. An agreement within 4 dB was seen between the measurement and the theoretical model.
- Also, the $\sqrt{F}$ variation of Z_T as predicted by Tini was seen

Finally, a few methodology recommendations are given in the last section of chapter 5 for the KAT team in future evaluation of coaxial cables Z_T.

6.2 Further Work

For global RFI mitigation in electronic systems, the two potential EMI sources should be considered as discussed in chapter 2. Briefly, the interference might come from the noise penetration through imperfections of the signal transport coaxial. The noise might also originate from poor protection of each instrument (insufficient shielding). Thus, we must consider the noise coupling at both parts of the configuration to mitigate the interference on the system properly. The Z_T characterisation of the coaxial cables identified in the system constitutes a first approach towards the RFI mitigation in cables. While this task is common practice in cable classification, it is not enough for EMI mitigation on complex systems. Imagine a long cable bundle coming from different building blocks, telescope or apertures arrays. Apart the mutual coupling between each cable, which is inevitable in most situations, the cable layout is also introducing unintentionally large loops in the circuit. The bigger the loop the more sensitive the system is to magnetic coupling. This increases the level of RFI susceptibility of the system. Although, the EMI mitigation depends primarily on cables Z_T, it is also a matter of cabling path and interface construction. Pursuing research on cable routing optimization and enclosure shielding effectiveness evaluation is therefore important for a systematic approach to complete RFI mitigation of the MeerKAT and the SKA projects.

References

[1] "South African SKA." http://www.ska.ac.za/meerkat/specsci.php.

[2] "An open invitation to the astronomical community to propose key project science with the south african square kilometre array precursor." http://www.ska.ac.za/temp/rfp_meerkat.pdf.

[3] C. Andrew, "RF dialects: Understanding each others technical lingo," Jun. 2010. www.iucaf.org/SSS2010/presentations/day2/Clegg(Units).ppt.

[4] S. W. Ellingson, "RFI mitigation and SKA," *Experimental Astronomy*, vol. 17, pp. 261–267, Jun. 2004.

[5] T. Benson, A. Duffy, and C. Cheng, "Assessing the performance of a current probe based method for determining surface transfer impedance," in *10th International Conference on Electromagnetic Compatibility*, no. 445, pp. 137–141, Sep. 1997.

[6] C. Paul, *Introduction to Electomagnetic Compatibility*. Wiley Interscience publication, 1992.

[7] F. M. Tesche, M. V. Ianozov, and T. Karlsson, *EMC Analysis Methods and Computational Models*. Wiley Interscience, 1997.

[8] P. A. Chatterton and M. A. Houlden, *EMC Electomagnetic Theory to Practical Design*. Wiley, 1992.

[9] B. Keiser, *Principles of Electromagnetic Compatibility*. Artech house, 3rd ed., 1987.

[10] R. Perez, *Handbook of Electromagnetic Compatibility*. Academic Press, 1995.

[11] S. Sali, "An improved model for the transfer impedance calculations of braided coaxial cables," *IEEE Transactions on Electromagnetic Compatibility*, vol. 33, pp. 139–143, May 1991.

[12] R. Tiedemann, "Current flow in coaxial braided cable shields," *IEEE Transactions on Electromagnetic Compatibility*, vol. 45, pp. 531– 537, Aug. 2003.

[13] T. Williams, *EMC for Product Designers*. Newnes, 2nd ed., 1996.

[14] C. Christopoulos, *Principles and Techniques of Electromagnetic Compatibility*. CRC Press, 1995.

[15] A. Tsaliovitch, *Cable Shielding For Electromagnetic Compatibility*. Kluwer Academic, 1995.

[16] D. A. Weston, "Transfert impedance and shielding effectiveness of a belden 8669 overbraided shielded cable compared to RG58 and RG214 from 0.25 MHz to 12 GHz," tech. rep. http://www.emcconsultinginc.com/docs/beldenTiAndSe.pdf.

[17] A. Morriello, T. Benson, A. Duffy, and C. Cheng, "Surface transfer impedance measurement: A comparison between current probe and pull-on braid methods for coaxial cables," *IEEE Transactions on Electromagnetic Compatibility*, vol. 40, pp. 69–76, Feb. 1998.

[18] H. C. Reader, R. H. Geschke, A. J. Otto, and J. Badenhorst, "Transfer impedance and EM bandgap structures in EMI suppression," in *Power Eng Conference SAUPEC 2008, 17th Southern African Univ.*, 2008.

[19] K. Casey and E. Vance, "EMP coupling through cable shields," *IEEE Transactions on Electromagnetic Compatibility*, vol. EMC-20, pp. 100–106, Feb. 1978.

[20] E. Vance, "Shielding effectiveness of braided-wire shields," *IEEE Transactions on Electromagnetic Compatibility*, vol. EMC-17, pp. 71–77, May 1975.

[21] S. Kurennoy, "Polarizabilities of an annular cut in the wall of an arbitrary thickness," *IEEE Transactions on Microwave Theory and Techniques*, vol. 44, pp. 1109–1114, Jul. 1996.

[22] L. O. Hoeft, "A simplifed relationship between surface transfer impedance and mode stirred chamber shielding effectiveness of cables and connectors," *International Symposium on EMC*, pp. 441–446, Sep. 2002.

[23] L. Halme, "Development of IEC cable shielding effectiveness standards," in *IEEE International Symposium on Electromagnetic Compatibility*, pp. 321–328, Aug. 1992.

[24] ISO/IEC 61000-4-21, *Electromagnetic Compatibility (EMC) Part 4-21: Testing and Measurement Techniques - Reverberation Chamber Test Methods*. Oct. 2009. Draft version.

[25] ISO/IEC 61726, *Cable Assemblies, Cables, Connectors and Passive Microwave Components - Screening Attenuation Measurement by the Reverberation Chamber Method*. 2nd ed., Nov. 1999.

[26] M. T. Ma, "Understanding reverberating chambers as an alternative facility for EMC testing," *Journal of electromagnetic waves and applications*, vol. 2, no. 3/4, pp. 339–351, 1988.

[27] B. S. Guru and H. R. Hiziruglu, *Electromagnetic Field Theory Fundamentals*. Cambridge University Press, 2nd ed., 2004.

[28] J. Nijenhuis, *Characterization and Application of a Reverberating Chamber*. University of Technology of Eindhoven, Nov. 2009. http://alexandria.tue.nl/repository/books/657752.pdf.

[29] M. Bäckström, O. Lundén, and P. Kildal, "Reverberation chambers for EMC susceptibility and emission analyses," *The Rev. of. Radio Science*, pp. 429–452, 1999-2002.

[30] J. Ladbury and G. Koepke, "Reverberation chamber relationships: Corrections and improvements or three wrongs can (almost) make a right," in *IEEE International Symposium on Electromagnetic Compatibility*, vol. 1, pp. 1–6, 1999.

[31] K. Madsen, P. Hallbjorner, and C. Orlenius, "Models for the number of independent samples in reverberation chamber measurements with mechanical, frequency, and combined stirring," *Antennas and Wireless Propagation Letters, IEEE*, vol. 3, pp. 48–51, Dec. 2004.

[32] C. Lemoine, P. Besnier, and M. Drissi, "Advanced method for estimating number of independent samples available with stirrer in reverberation chamber," *Electronics Letters*, vol. 43, pp. 861–862, Feb. 2007.

[33] O. Lundén and M. Bäckström, "Stirrer efficiency in FOA reverberation chambers. Evaluation of correlation coefficients and chi-squared tests," in *IEEE International Symposium on Electromagnetic Compatibility*, vol. 1, pp. 11–16, 2000.

[34] H. Krauthauser, T. Winzerling, and J. Nitsch, "Statistical interpretation of autocorrelation coefficients for fields in mode-stirred chambers," in *International Symposium on Electromagnetic Compatibility*, vol. 2, pp. 550–555, Aug. 2005.

[35] J. Kostas and B. Boverie, "Statistical model for a mode-stirred chamber," *IEEE Transactions on Electromagnetic Compatibility*, vol. 33, pp. 366–370, Nov. 1991.

[36] T. Harrington, "Total-radiated-power-based OATS-equivalent emissions testing in reverberation chambers and GTEM cells," in *IEEE International Symposium on Electromagnetic Compatibility*, vol. 1, pp. 23–28, 2000.

[37] G. P. Wiid, "Investigating cost-effective EMC methods," Master's thesis, University of Stellenbosch, Dec. 2005.

[38] K. Harima, "Radiated emission measurement of small EUT by using a reverberation chamber," in *IEEE International Symposium on Electromagnetic Compatibility*, vol. 1, pp. 471–474, May 2003.

[39] NPL, *Certificate of Calibration*. Laplace Instruments LTD, Oct. 2007.

[40] N. Ebertsohn, R. Geschke, and H. Reader, "Cable trays in EMC: Measurement and modeling to 30 MHz," *IEEE Transactions on Electromagnetic Compatibility*, vol. 49, pp. 346–353, May 2007.

[41] Rohde. and Schwarz, *ZVB Vector Network Analyzers Product Brochure*, Dec. 2007. ver 6.0.

[42] L. Bai, L. Wang, B. Wang, and J. Song, "Reverberation chamber modeling using FDTD," in *IEEE International Symposium on Electromagnetic Compatibility*, vol. 1, pp. 7–11, 1999.

[43] T. Aurand, J. Dawson, A. Marvin, and M. Robinson, "Reverberation chamber calibration: Differences in results when using a slot instead of a dipole antenna," in *IEEE International Symposium on Electromagnetic Compatibility*, pp. 1–4, Jul. 2007.

[44] L. R. Arnaut, *Uncertainty Reduction and Decorrelation of Mode-Stirred Reverberation Chamber Data Using Transformation and Expansion Techniques*. NPL Report CETM 21, Jun. 2000. http://publications.npl.co.uk/npl_web/pdf/cetm21.pdf.

[45] C. Lemoine, P. Besnier, and M. Drissi, "Estimating the effective sample size to select independent measurements in a reverberation chamber," *IEEE Transactions on Electromagnetic Compatibility*, vol. 50, no. 2, 2008.

[46] J. O'Neil, *EMC*. IEEE EMC Society Newsletter no. 229, 2011. http://ewh.ieee.org/soc/emcs/acstrial/newsletters/spring11/.

[47] A. Fourie, O. Givati, and A. Clark, "Simple technique for the measurement of the transfer impedance of variable length coaxial interconnecting leads," *IEEE Transactions on Electromagnetic Compatibility*, vol. 40, pp. 163–166, May 1998.

[48] L. Hoeft and J. Hofstra, "Measured electromagnetic shielding performance of commonly used cables and connectors," *IEEE Transactions on Electromagnetic Compatibility*, vol. 30, pp. 260–275, Aug. 1988.

Appendices

APPENDIX A

Polarizabilities of Selected Apertures

Aperture Shape	α_e	α_{mx}	α_{my}
Circle (diameter d)	$\frac{1}{12}d^3$	$\frac{1}{6}d^3$	$\frac{1}{6}d^3$
Ellipse	$\frac{\pi}{24}\frac{w^2 l}{E(e)}$	$\frac{\pi}{24}\frac{e^2 l^3}{K(e)-E(e)}$	$\frac{\pi}{24}\frac{e^2 l^3}{(l/w)^2 E(e)-K(e)}$
Narrow ellipse ($w \ll l$)	$\frac{\pi}{24}w^2 l$	$\frac{\pi}{24}\frac{l^3}{ln(4l/w)-1}$	$\frac{\pi}{24}w^2 l$
Narrow slit ($w \ll l$)	$\frac{\pi}{16}w^2 l$	$\frac{\pi}{24}\frac{l^3}{ln(4l/w)-1}$	$\frac{\pi}{16}w^2 l$

K(e) and E(e) are the complete elliptical integrals. We have:

$$K(e) = \int_0^{\pi/2} (1 - e^2 sin^2(\theta))^{1/2} d\theta$$

$$E(e) = \int_0^{\pi/2} (1 - e^2 sin^2(\theta))^{-1/2} d\theta$$

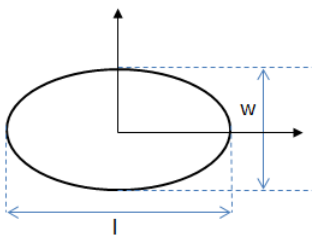

APPENDIX B

MATLAB Program Listing

B.1 Reverberation Chamber Calibration

```
%************************************************************************
%              CHARACTERISATION OF THE RVERBERATION CHAMBER
%              ____________________________________________
% Objectives:
%   1 – Calculation of the chamber attenuation
%   2 – Verification of the electric field uniformity
%   12 Novembre 2010
%************************************************************************

clear all;
close all;
clc;

% Load the S21 data at the 8 positions (8 corners of the working volume)
% Number of samples = 72 per revolution
%_____________________________________________________________________
[S11_A1,S11max_A1,S21_A1,S21max_A1,S12_A1,S12max_A1,S22_A1,S22max_A1,F] = ZVBSegFRead('posA1.s2p',72);
[S11_A2,S11max_A2,S21_A2,S21max_A2,S12_A2,S12max_A2,S22_A2,S22max_A2]   = ZVBSegFRead('posA2.s2p',72);
[S11_A3,S11max_A3,S21_A3,S21max_A3,S12_A3,S12max_A3,S22_A3,S22max_A3]   = ZVBSegFRead('posA3.s2p',72);
[S11_A4,S11max_A4,S21_A4,S21max_A4,S12_A4,S12max_A4,S22_A4,S22max_A4]   = ZVBSegFRead('posA4.s2p',72);
[S11_B1,S11max_B1,S21_B1,S21max_B1,S12_B1,S12max_B1,S22_B1,S22max_B1]   = ZVBSegFRead('posB1.s2p',72);
[S11_B2,S11max_B2,S21_B2,S21max_B2,S12_B2,S12max_B2,S22_B2,S22max_B2]   = ZVBSegFRead('posB2.s2p',72);
[S11_B3,S11max_B3,S21_B3,S21max_B3,S12_B3,S12max_B3,S22_B3,S22max_B3]   = ZVBSegFRead('posB3.s2p',72);
[S11_B4,S11max_B4,S21_B4,S21max_B4,S12_B4,S12max_B4,S22_B4,S22max_B4]   = ZVBSegFRead('posB4.s2p',72);
```

```
% Antenna efficiency of KLPDA
%-------------------------------------------------
D_KLPDA2 = 0.75;
D_KLPDA4 = 0.75;

%%                S21 AND ANTENNA MISMATCHES CALCULATION
%-------------------------------------------------------------------------------

% Antenna mismatches LPDA Tx and Rx (1 - s11^2) and (1 - s22^2)
%-------------------------------------------------------------
LossKLPDA1_A1 = 1 - abs(S11_A1).^2;
LossKLPDA1_A2 = 1 - abs(S11_A2).^2;
LossKLPDA1_A3 = 1 - abs(S11_A3).^2;
LossKLPDA1_A4 = 1 - abs(S11_A4).^2;
LossKLPDA1_B1 = 1 - abs(S11_B1).^2;
LossKLPDA1_B2 = 1 - abs(S11_B2).^2;
LossKLPDA1_B3 = 1 - abs(S11_B3).^2;
LossKLPDA1_B4 = 1 - abs(S11_B4).^2;

LossKLPDA2_A1 = 1 - abs(S22_A1).^2;
LossKLPDA2_A2 = 1 - abs(S22_A2).^2;
LossKLPDA2_A3 = 1 - abs(S22_A3).^2;
LossKLPDA2_A4 = 1 - abs(S22_A4).^2;
LossKLPDA2_B1 = 1 - abs(S22_B1).^2;
LossKLPDA2_B2 = 1 - abs(S22_B2).^2;
LossKLPDA2_B3 = 1 - abs(S22_B3).^2;
LossKLPDA2_B4 = 1 - abs(S22_B4).^2;

S21_A1_dB =20*log10(S21_A1);
S21_A2_dB =20*log10(S21_A2);
S21_A3_dB =20*log10(S21_A3);
S21_A4_dB =20*log10(S21_A4);
S21_B1_dB =20*log10(S21_B1);
S21_B2_dB =20*log10(S21_B2);
S21_B3_dB =20*log10(S21_B3);
S21_B4_dB =20*log10(S21_B4);

%%                          CHAMBER CALIBRATION FACTOR
%                           --------------------------
% Att_CH = Prx_av/Ptx_av
%-------------------------------------------------------------------------------
CCF_A1 = (S21_A1.^2)./(LossKLPDA1_A1.*LossKLPDA2_A1.*D_KLPDA2.*D_KLPDA4);
CCF_A2 = (S21_A2.^2)./(LossKLPDA1_A2.*LossKLPDA2_A2.*D_KLPDA2.*D_KLPDA4);
CCF_A3 = (S21_A3.^2)./(LossKLPDA1_A3.*LossKLPDA2_A3.*D_KLPDA2.*D_KLPDA4);
CCF_A4 = (S21_A4.^2)./(LossKLPDA1_A4.*LossKLPDA2_A4.*D_KLPDA2.*D_KLPDA4);
CCF_B1 = (S21_B1.^2)./(LossKLPDA1_B1.*LossKLPDA2_B1.*D_KLPDA2.*D_KLPDA4);
CCF_B2 = (S21_B2.^2)./(LossKLPDA1_B2.*LossKLPDA2_B2.*D_KLPDA2.*D_KLPDA4);
CCF_B3 = (S21_B3.^2)./(LossKLPDA1_B3.*LossKLPDA2_B3.*D_KLPDA2.*D_KLPDA4);
CCF_B4 = (S21_B4.^2)./(LossKLPDA1_B4.*LossKLPDA2_B4.*D_KLPDA2.*D_KLPDA4);

CCF_A1_dB = 10*log10(CCF_A1);
CCF_A2_dB = 10*log10(CCF_A2);
CCF_A3_dB = 10*log10(CCF_A3);
CCF_A4_dB = 10*log10(CCF_A4);
CCF_B1_dB = 10*log10(CCF_B1);
CCF_B2_dB = 10*log10(CCF_B2);
```

```
CCF_B3_dB = 10*log10(CCF_B3);
CCF_B4_dB = 10*log10(CCF_B4);

% The final chamber loss in dB is the average of the 8 losses above
CCF_Mean = (CCF_A1 + CCF_A2 + CCF_A3 + CCF_A4 + CCF_B1 + CCF_B2 + CCF_B3 + CCF_B4)/8;
CCF_Mean_dB = 10*log10(CCF_Mean);

%%                          INSERTION LOSS
%                           ______________
% CCF = Prxmax/Ptxmax
%-------------------------------------------------------------------------
%                S21 AND ANTENNA MISMATCHES CALCULATION
%-------------------------------------------------------------------------
LossKLPDA1max_A1 = 1 - abs(S11max_A1).^2;
LossKLPDA1max_A2 = 1 - abs(S11max_A2).^2;
LossKLPDA1max_A3 = 1 - abs(S11max_A3).^2;
LossKLPDA1max_A4 = 1 - abs(S11max_A4).^2;
LossKLPDA1max_B1 = 1 - abs(S11max_B1).^2;
LossKLPDA1max_B2 = 1 - abs(S11max_B2).^2;
LossKLPDA1max_B3 = 1 - abs(S11max_B3).^2;
LossKLPDA1max_B4 = 1 - abs(S11max_B4).^2;

LossKLPDA2max_A1 = 1 - abs(S22max_A1).^2;
LossKLPDA2max_A2 = 1 - abs(S22max_A2).^2;
LossKLPDA2max_A3 = 1 - abs(S22max_A3).^2;
LossKLPDA2max_A4 = 1 - abs(S22max_A4).^2;
LossKLPDA2max_B1 = 1 - abs(S22max_B1).^2;
LossKLPDA2max_B2 = 1 - abs(S22max_B2).^2;
LossKLPDA2max_B3 = 1 - abs(S22max_B3).^2;
LossKLPDA2max_B4 = 1 - abs(S22max_B4).^2;

IL_A1 = (S21max_A1.^2)./(LossKLPDA1max_A1.*LossKLPDA2max_A1.*D_KLPDA2.*D_KLPDA4);
IL_A2 = (S21max_A2.^2)./(LossKLPDA1max_A2.*LossKLPDA2max_A2.*D_KLPDA2.*D_KLPDA4);
IL_A3 = (S21max_A3.^2)./(LossKLPDA1max_A3.*LossKLPDA2max_A3.*D_KLPDA2.*D_KLPDA4);
IL_A4 = (S21max_A4.^2)./(LossKLPDA1max_A4.*LossKLPDA2max_A4.*D_KLPDA2.*D_KLPDA4);
IL_B1 = (S21max_B1.^2)./(LossKLPDA1max_B1.*LossKLPDA2max_B1.*D_KLPDA2.*D_KLPDA4);
IL_B2 = (S21max_B2.^2)./(LossKLPDA1max_B2.*LossKLPDA2max_B2.*D_KLPDA2.*D_KLPDA4);
IL_B3 = (S21max_B3.^2)./(LossKLPDA1max_B3.*LossKLPDA2max_B3.*D_KLPDA2.*D_KLPDA4);
IL_B4 = (S21max_B4.^2)./(LossKLPDA1max_B4.*LossKLPDA2max_B4.*D_KLPDA2.*D_KLPDA4);

IL_A1_dB = 10*log10(IL_A1);
IL_A2_dB = 10*log10(IL_A2);
IL_A3_dB = 10*log10(IL_A3);
IL_A4_dB = 10*log10(IL_A4);
IL_B1_dB = 10*log10(IL_B1);
IL_B2_dB = 10*log10(IL_B2);
IL_B3_dB = 10*log10(IL_B3);
IL_B4_dB = 10*log10(IL_B4);

% The final chamber loss in dB is the average of the 8 losses above
IL_Mean      = (IL_A1 + IL_A2 + IL_A3 + IL_A4 + IL_B1 + IL_B2 + IL_B3 + IL_B4)/8;
IL_Mean_dB   = 10*log10(IL_Mean);

%%                             ELECTRIC FIELD
%                              ______________
% 1 - Calculation of EField for the 8 position
```

```
% 2 — Calculation of the Efield variation in the working volume
%————————————————————————————————————————————————————————————

% input power in Port i in watt
Pin = 1e-3;
lambda = 3e8./F;

% The maximum power received over one revolution
PRx_A1_max = (S21max_A1.^2*Pin)./(LossKLPDA1max_A1.*D_KLPDA4);
PRx_A2_max = (S21max_A2.^2*Pin)./(LossKLPDA1max_A2.*D_KLPDA4);
PRx_A3_max = (S21max_A3.^2*Pin)./(LossKLPDA1max_A2.*D_KLPDA4);
PRx_A4_max = (S21max_A4.^2*Pin)./(LossKLPDA1max_A3.*D_KLPDA4);
PRx_B1_max = (S21max_B1.^2*Pin)./(LossKLPDA1max_B1.*D_KLPDA4);
PRx_B2_max = (S21max_B2.^2*Pin)./(LossKLPDA1max_B2.*D_KLPDA4);
PRx_B3_max = (S21max_B3.^2*Pin)./(LossKLPDA1max_B3.*D_KLPDA4);
PRx_B4_max = (S21max_B4.^2*Pin)./(LossKLPDA1max_B4.*D_KLPDA4);

% Electric field max in uV
E_A1_max   = (8*pi./lambda).*sqrt(5*PRx_A1_max./D_KLPDA4)*1e6;
E_A2_max   = (8*pi./lambda).*sqrt(5*PRx_A2_max./D_KLPDA4)*1e6;
E_A3_max   = (8*pi./lambda).*sqrt(5*PRx_A3_max./D_KLPDA4)*1e6;
E_A4_max   = (8*pi./lambda).*sqrt(5*PRx_A4_max./D_KLPDA4)*1e6;
E_B1_max   = (8*pi./lambda).*sqrt(5*PRx_B1_max./D_KLPDA4)*1e6;
E_B2_max   = (8*pi./lambda).*sqrt(5*PRx_B2_max./D_KLPDA4)*1e6;
E_B3_max   = (8*pi./lambda).*sqrt(5*PRx_B3_max./D_KLPDA4)*1e6;
E_B4_max   = (8*pi./lambda).*sqrt(5*PRx_B4_max./D_KLPDA4)*1e6;

E_A1_max_dBuV = 20*log10(E_A1_max);
E_A2_max_dBuV = 20*log10(E_A2_max);
E_A3_max_dBuV = 20*log10(E_A3_max);
E_A4_max_dBuV = 20*log10(E_A4_max);
E_B1_max_dBuV = 20*log10(E_B1_max);
E_B2_max_dBuV = 20*log10(E_B2_max);
E_B3_max_dBuV = 20*log10(E_B3_max);
E_B4_max_dBuV = 20*log10(E_B4_max);

% The average power received over one revolution
PRx_A1 = (S21_A1.^2*Pin)./(LossKLPDA1_A1.*D_KLPDA4);
PRx_A2 = (S21_A2.^2*Pin)./(LossKLPDA1_A2.*D_KLPDA4);
PRx_A3 = (S21_A3.^2*Pin)./(LossKLPDA1_A2.*D_KLPDA4);
PRx_A4 = (S21_A4.^2*Pin)./(LossKLPDA1_A3.*D_KLPDA4);
PRx_B1 = (S21_B1.^2*Pin)./(LossKLPDA1_B1.*D_KLPDA4);
PRx_B2 = (S21_B2.^2*Pin)./(LossKLPDA1_B2.*D_KLPDA4);
PRx_B3 = (S21_B3.^2*Pin)./(LossKLPDA1_B3.*D_KLPDA4);
PRx_B4 = (S21_B4.^2*Pin)./(LossKLPDA1_B4.*D_KLPDA4);

% Average E-field
neta = 120*pi;
N = 8;
Factor = 15/16*sqrt(pi/3)*(gamma(3*N)*sqrt(3*N)/gamma(3*N+1/2));

% Electric field in uV
E_A1   = sqrt(8*pi*neta*PRx_A1./(lambda.^2))*1e6*Factor;
E_A2   = sqrt(8*pi*neta*PRx_A2./(lambda.^2))*1e6*Factor;
E_A3   = sqrt(8*pi*neta*PRx_A3./(lambda.^2))*1e6*Factor;
E_A4   = sqrt(8*pi*neta*PRx_A4./(lambda.^2))*1e6*Factor;
```

```
E_B1    = sqrt(8*pi*neta*PRx_B1./(lambda.^2))*1e6*Factor;
E_B2    = sqrt(8*pi*neta*PRx_B2./(lambda.^2))*1e6*Factor;
E_B3    = sqrt(8*pi*neta*PRx_B3./(lambda.^2))*1e6*Factor;
E_B4    = sqrt(8*pi*neta*PRx_B4./(lambda.^2))*1e6*Factor;

E_A1_dBuV = 20*log10(E_A1);
E_A2_dBuV = 20*log10(E_A2);
E_A3_dBuV = 20*log10(E_A3);
E_A4_dBuV = 20*log10(E_A4);
E_B1_dBuV = 20*log10(E_B1);
E_B2_dBuV = 20*log10(E_B2);
E_B3_dBuV = 20*log10(E_B3);
E_B4_dBuV = 20*log10(E_B4);

%% ESTIMATION OF THE ELECTRIC FIELD MEAN
%-----------------------------------------
E_Mean = (E_A1 + E_A2 + E_A3 + E_A4 + E_B1 + E_B2 + E_B3 + E_B4)/8;
E_Mean_dBuV = 20*log10(E_Mean);

E_Mean_max = (E_A1_max + E_A2_max + E_A3_max + E_A4_max + E_B1_max + E_B2_max + E_B3_max + E_B4_max)/8;
E_Mean_max_dBuV = 20*log10(E_Mean_max);

% Normalised mean Electric field
E_A1_Var_dB = E_A1_dBuV - E_Mean_dBuV;
E_A2_Var_dB = E_A2_dBuV - E_Mean_dBuV;
E_A3_Var_dB = E_A3_dBuV - E_Mean_dBuV;
E_A4_Var_dB = E_A4_dBuV - E_Mean_dBuV;
E_B1_Var_dB = E_B1_dBuV - E_Mean_dBuV;
E_B2_Var_dB = E_B2_dBuV - E_Mean_dBuV;
E_B3_Var_dB = E_B3_dBuV - E_Mean_dBuV;
E_B4_Var_dB = E_B4_dBuV - E_Mean_dBuV;

% normalised Max Electric field
E_A1_Var_max_dB = E_A1_max_dBuV - E_Mean_max_dBuV;
E_A2_Var_max_dB = E_A2_max_dBuV - E_Mean_max_dBuV;
E_A3_Var_max_dB = E_A3_max_dBuV - E_Mean_max_dBuV;
E_A4_Var_max_dB = E_A4_max_dBuV - E_Mean_max_dBuV;
E_B1_Var_max_dB = E_B1_max_dBuV - E_Mean_max_dBuV;
E_B2_Var_max_dB = E_B2_max_dBuV - E_Mean_max_dBuV;
E_B3_Var_max_dB = E_B3_max_dBuV - E_Mean_max_dBuV;
E_B4_Var_max_dB = E_B4_max_dBuV - E_Mean_max_dBuV;

%%                          STANDARD DEVIATION CALCULATION
%-------------------------------------------------------------------------
E = [E_A1_max'; E_A2_max'; E_A3_max'; E_A4_max'; E_B1_max'; E_B2_max'; E_B3_max'; E_B4_max']*1e-6;
% standard deviation
Std_Dev = std(E);

% standard deviation in dB
Std_Dev_dB = 20*log10((Std_Dev' + E_Mean*1e-6)./(E_Mean*1e-6));

% IEC Standard limit
%--------------------
x = [100 400 500 600 1300]*1e6;
y = [4 3 3 3 3];
IEC_Limite = interp1(x,y,F);
```

```
%%                                  PLOTTING
%                                   ________
% 1 - Attenuation of the chamber (mean)
% 2 - E field
% 3 - E field variation
%-------------------------------------------------------------------------

% Mean E-field
figure;
plot(F,E_A1_dBuV);
hold on;
grid on;
plot(F,E_A2_dBuV,'r');
plot(F,E_A3_dBuV,'m');
plot(F,E_A4_dBuV,'g');
plot(F,E_B1_dBuV,'-.b');
plot(F,E_B2_dBuV,'-.r');
plot(F,E_B3_dBuV,'-.m');
plot(F,E_B4_dBuV,'-.g');
plot(F,E_Mean_dBuV,'k');
title('MEAN ELECTRIC FIELD');
xlabel('Frequency in Hz');
ylabel('E-field in dBuV/m');

% Max E-field
figure;
plot(F,E_A1_max_dBuV);
hold on;
grid on;
plot(F,E_A2_max_dBuV,'r');
plot(F,E_A3_max_dBuV,'m');
plot(F,E_A4_max_dBuV,'g');
plot(F,E_B1_max_dBuV,'-.b');
plot(F,E_B2_max_dBuV,'-.r');
plot(F,E_B3_max_dBuV,'-.m');
plot(F,E_B4_max_dBuV,'-.g');
plot(F,E_Mean_max_dBuV,'k');
title('MAX ELECTRIC FIELD');
xlabel('Frequency in Hz');
ylabel('E-field in dBuV/m');

% Normalised mean E-field
figure;
plot(F,E_A1_Var_dB);
hold on;
grid on;
plot(F,E_A2_Var_dB,'r');
plot(F,E_A3_Var_dB,'m');
plot(F,E_A4_Var_dB,'g');
plot(F,E_B1_Var_dB,'-.b');
plot(F,E_B2_Var_dB,'-.r');
plot(F,E_B3_Var_dB,'-.m');
plot(F,E_B4_Var_dB,'-.g');
title('NORMALISED MEAN ELECTRIC FIELD');
xlabel('Frequency in Hz');
```

```
ylabel('E-field in dBuV/m');

% Normalised max E-field
figure;
plot(F,E_A1_Var_max_dB);
hold on;
grid on;
plot(F,E_A2_Var_max_dB,'r');
plot(F,E_A3_Var_max_dB,'m');
plot(F,E_A4_Var_max_dB,'g');
plot(F,E_B1_Var_max_dB,'-.b');
plot(F,E_B2_Var_max_dB,'-.r');
plot(F,E_B3_Var_max_dB,'-.m');
plot(F,E_B4_Var_max_dB,'-.g');
title('NORMALISED MAX ELECTRIC FIELD');
xlabel('Frequency in Hz');
ylabel('E-field in dBuV/m');

% Standard deviation
figure;
plot(F,Std_Dev_dB,'-.r' );
hold on;
grid on;
plot(F,IEC_Limite);
```

B.2 Rohde and Schwarz s3p Reader Function

```
function [S11,S11max,S21,S21max,S12,S12max,S22,S22max,F] = ZVBSegFRead(Filename,N_Pts);
%-------------------------------------------------------------------------
%                  ZVB Segmented frequency Data Reading
%                  ------------------------------------
% Filename  : *.s2p file from segemented frequency measurement on ZVB-8
% Output    : Averaged and Max S-Param in the order :
%             S11, S11max, S21, S21max, S12, S12max, S22, S22max, F
% Input     : - Filename
%             - The number of samples per revolution (N_Pts)
%-------------------------------------------------------------------------

DataReg = importdata(Filename,' ',5);

% calculation of the frequency points number
F_Pts  = size(DataReg.data(:,1))/N_Pts;

for k = 1:F_Pts(1)
    n = (k - 1)*N_Pts + 1;

    % Compute the average of the N_Pts values
    S11(k,1) = mean(abs(DataReg.data(n:n+N_Pts-1,2) + 1i*DataReg.data(n:n+N_Pts-1,3)));
    S21(k,1) = mean(abs(DataReg.data(n:n+N_Pts-1,4) + 1i*DataReg.data(n:n+N_Pts-1,5)));
    S12(k,1) = mean(abs(DataReg.data(n:n+N_Pts-1,6) + 1i*DataReg.data(n:n+N_Pts-1,7)));
    S22(k,1) = mean(abs(DataReg.data(n:n+N_Pts-1,8) + 1i*DataReg.data(n:n+N_Pts-1,9)));

    % load the N_Pts S21, S11 and S22 data for one frequency
```

```
    S11_tmp = abs(DataReg.data(n:n+N_Pts-1,2) + i*DataReg.data(n:n+N_Pts-1,3));
    S21_tmp = abs(DataReg.data(n:n+N_Pts-1,4) + i*DataReg.data(n:n+N_Pts-1,5));
    S12_tmp = abs(DataReg.data(n:n+N_Pts-1,6) + i*DataReg.data(n:n+N_Pts-1,7));
    S22_tmp = abs(DataReg.data(n:n+N_Pts-1,8) + i*DataReg.data(n:n+N_Pts-1,9));

    % Find S21max over the N_Pts data
    % Find the S11 and S22 corresponding to that S21max
    [S21max(k,1),I(k,1)] = max(S21_tmp);
     S12max(k,1) = max(S12_tmp);
     S11max(k,1) = S11_tmp(I(k,1));
     S22max(k,1) = S22_tmp(I(k,1));

    F(k,1)    = mean(DataReg.data(n:n+N_Pts-1,1));
end
```

B.3 Coaxial Air-line Z_T

```
%==========================================================================
%
%   SHIELDING EFFECTIVENESS INVESTIGATION USING A REVERBERATION CHAMBER
%
%==========================================================================
% Frequency range : 300MHz - 1300MHz
%-----------------
% Input power     : 25 dBm
% Measurement BandWidth : 100 Hz
%==========================================================================
close all;
clear all;
clc;

%% Initialisation
%-----------------
% LPDA efficiency
Ant_eff = 0.75;

% Length of the air-line
L_CBL = 1.304;

%% USER Prompt
%-------------------
filename = input('Enter the file name : ','s');

%% Load the chamber's parameters and the Current Probe Zt
%-------------------------------------------------------
% Antenna calibration factor obtained for RC calibration
IL  = importdata('data\IL_efficiency_0,75.csv');

% Transfer impedance of the current probe (EMCO 50999) in dBOhm
%--------------------------------------------------------------
EMCO = importdata('data\EMCO_Probe_Zt.csv');

% measurement's data filename (from the RC)
```

```
file1 = strcat(filename,'_HF.s2p');
file1 = strcat('Measurement\',file1);
% measurement's data filename (from the field to wire method)
file2 = strcat(filename,'_LF.s3p');
file2 = strcat('Measurement\',file2);

% LOAD DATA
%------------
[S11_CBL,S11max_CBL,S21_CBL,S21max_CBL,S12_CBL,S12max_CBL,S22_CBL,S22max_CBL,F_HF] = ZVBSegFRead(file1,72);
[F_LF,S11_C,S12_C,S13_C,S21_C,S22_C,S23_C,S31_C,S32_C,S33_C] = ZVBRead_s3p(file2);

%% ========================================================================
%                       HIGH FREQUENCY PART OF ZT
%=========================================================================
% Resampling IL
%---------------
IL_F     = IL(:,1);
IL_Data  = IL(:,2);
IL       = interp1(IL_F,IL_Data,F_HF);

% Mismatches evaluation
%-----------------------
% antenna input
Ant_mis_CBL  = 1 - S22max_CBL.^2;

% Mismatches at the input of the cable
CBL_Mis  = 1 - S11max_CBL.^2;

%%  SHIELDING EFECTIVENESS CALCULATION
%-------------------------------------
% Corrected Shielding effectiveness of the cable
%-------------------------------------------------
SE_CBL = S21max_CBL.^2./(Ant_eff.*Ant_mis_CBL.*CBL_Mis.*IL);

%% HF TRANSFER IMPEDANCE
%-----------------------
% Boilot and Eicher Foramulation
Z1 = 50;
Z2 = 377;
Zt_HF  = sqrt(2*Z1*Z2*SE_CBL);

%% ========================================================================
%                       LOW FREQUENCY PART OF ZT
%=========================================================================

% Resampling The EMCO Zt
%------------------------
EMCO_F      = EMCO(:,1);
EMCO_Ztt_dB = EMCO(:,2);
EMCO_Ztt    = 10.^(EMCO_Ztt_dB/20);
Ztt         = interp1(EMCO_F,EMCO_Ztt,F_LF);

% CORRECTION FACTOR
%-------------------
er = 2.25;
lambda_0 = 3e8./F_LF;
```

```
B0 = 2*pi./lambda_0;
C = cos(sqrt(er)*B0*L_CBL) - cos(B0*L_CBL);
S = sqrt(er).*B0.*sin(sqrt(er).*B0.*L_CBL) - B0.*sin(B0.*L_CBL);

N = (sqrt(er)*B0).^2 - B0.^2;
M = sqrt(er*(B0.^2).*(C.^2) + S.^2);

CF = N./M;

% TRANSFER IMPEDANCE OF THE CABLE
%-------------------------------------
Zt_C = 4*Ztt.*abs(S21_C).*CF./abs(S31_C);

% Resonant frequency
%---------------------
F_res = 3e8/(L_CBL*4);
F_step   = (F_res - F_LF(1))/501;
F        = [F_LF(1):F_step:F_res];

% LF part of Zt up to F_res
%----------------------------
Zt_LF    = interp1(F_LF,abs(Zt_C),F);

%% ========================================================================
%                            THEORETICAL VARIATION
%-------------------------------------------------------------------------
% The transfer impedance at high frequency is reduced to Ztot = jM12w
%-------------------------------------------------------------------------

% Radius of the air-line
% (a : inner radius | b : outer radius)
%-----------------------------------------
a = (7.19e-3)/2;
b = (7.94e-3)/2;

% Radius of the hole
%---------------------
a_Hole = (2.9e-3)/2;

% Thickness D of the sheath
%----------------------------
D = b - a;

% Permeability u
%-----------------
u0 = 4*pi*1e-7;

F_calc = [F_LF(1):1e4:F_HF(length(F_HF))];

% Conductivity of a copper, brass
%----------------------------------
sigma_IACS = 5.8108e+7      % IACS at 20 deg C
sigma = 0.2*sigma_IACS;     % for brass C85400 (recommended by Wessel Croucamp)
                            % 20% IACS

Zt_calc = Zt_theory(F_calc,a_Hole,a,D,L_CBL,sigma);
```

```
%% INTERPOLATION OF ZT AT HF
%-------------------------------
% Method: Least mean square
%-------------------------------

% Definition of the data to be adjusted
%-----------------------------------------
x = [10e6:10e6:1.3e9];
X = log10(F_HF);
Y = 20*log10(Zt_HF);

% The means
%-----------------------
X_m = mean(X);
Y_m = mean(Y);

% Calculation of the LMS coefficients
%---------------------------------------
n = length(X);
A = (n*sum(X.*Y) - sum(X)*sum(Y))/(n*sum(X.^2) - sum(X).^2);
B = Y_m - A*X_m;

% The approximated Zt from
%-------------------------------
Zt_Approx = x.^(A/20).*(10^(B/20));

%% COMBINING THE 2 TRANSFER IMPEDANCE
%---------------------------------------
% by interpolation
%------------------
Zt_Freq = [F' ; F_HF(:,1)];
Zt_full = [Zt_LF' ; Zt_HF];
Freq    = [300e3:500e3:1000e6];
Zt_CBL  = interp1(Zt_Freq,Zt_full,Freq);

%% PLOTTING
%----------
% Tranfer impedance
figure;
semilogx(F_calc,20*log10(abs(Zt_calc)),'-.k');
grid on;
hold on;
semilogx(x,20*log10(Zt_Approx),'r');
semilogx(F,20*log10(Zt_LF));
semilogx(F_HF,20*log10(Zt_HF));
legend('Vance Zt Model','Slope of the Zt measurement');
xlabel('Frequency in Hz');
ylabel('Transfer impedance in dBOhm\m');
```

B.4 Coaxial Air-line Theoretical Function

```
function [Zt] = Zt_theory(F,Radius_hole,Inner_radius_tube,Thickness_tube,Length_tube,sigma)

% Permeability u
%----------------
u0 = 4*pi*1e-7;
ur = 1;
u = u0*ur;

%%                      SKIN DEPTH EFFECT
%-------------------------------------------------------------------------
% Skin depth
skin = 1./sqrt(pi*F*u*sigma);

% DC Resistance
M = (1+i)*Thickness_tube./skin;
Rdc = 1/(2*pi*sigma*Inner_radius_tube*Thickness_tube);

% Zt of the tubular shield
Zt_DC = Rdc.*M./sinh(M);

%%                  COUPLING THROUGH APERTURE (circular hole)
%-------------------------------------------------------------------------
% M12 = u0*alpha_eff/(pi*D)^2   D = diameter of the shield
% with alpha_eff = 3/2 alpham
% alpham = 4/3*radius_hole^3;
%-------------------------------------------------------------------------

% mutual inductance using alpha_m_eff
%-------------------------------------

D_Shield = 2*(Inner_radius_tube + Thickness_tube);

M12 = 2*u0*Radius_hole.^3/(pi*D_Shield)^2;

Zt_Hole = M12*2*pi*F;

%%                  TRANSFER IMPEDANCE OF THE AIR-LINE
%-------------------------------------------------------------------------

Zt = abs(Zt_DC) + i*Zt_Hole;
```

B.5 OATS E-field Equivalent Estimation

```
%=========================================================================
%
%                          OATS E-FIELD ESTIMATION
%
%=========================================================================

clear all;
close all;
clc;
```

```
%%   LOADING DATA
%_________________

% Antenna efficiency (LPDA)
%_____________________________
A_eff = 0.75;

% Cable loss
%_______________
S_Cable = importdata('SP_cable2.s2p',' ',5);
Loss_C = abs(S_Cable.data(:,4) + 1i*S_Cable.data(:,5));

% Chamber Insertion Loss (IL)
%_________________________________
IL_tmp = csvread('IL_efficiency_0,75.csv');

% Voltage files from the SA
%_____________________________
V_dbuV  = csvread('data_V.csv');    % Vertical Pol   (Z axis)
H1_dbuV = csvread('data_H1.csv');   % Horizontal Pol (X axis)
H2_dbuV = csvread('data_H2.csv');   % Horizontal Pol (Y axis)
Freq    = H2_dbuV(:,1);

% Chamber Loading Factor
%________________________
CLF = csvread('CLF_ERS.csv');

% Calibration's data
%____________________
C_Ver  = importdata('1552.ver');
C_Hor  = importdata('1552.hor');
C_freq = [30e6:2e6:1000e6];

% OATS parameters
%_________________
h = 0.8;
S = 3;
H = [1:0.1:4];

%%    PROCESS DATA
%__________________
% Find peak value of the data
%_____________________________________
w = 1;
k = 1;

while(w < length(Freq))
    F(k) = Freq(w);
    VdB_Peak(k,1)  = V_dbuV(w,2);
    H1dB_Peak(k,1) = H1_dbuV(w,2);
    H2dB_Peak(k,1) = H2_dbuV(w,2);
    w = w + 10;
    k = k+1;
end

% Normalisation of all data to the Freq range of the measurement
```

```
%-------------------------------------------------------------------
IL      = interp1(IL_tmp(:,1),IL_tmp(:,2),F);
Loss_C  = interp1(S_Cable.data(:,1),Loss_C,F);
CLF     = interp1(CLF(:,1),CLF(:,2),F);
C_Ver   = interp1(C_freq,C_Ver,F);
C_Hor   = interp1(C_freq,C_Hor,F);
IL = IL';
Loss_C = Loss_C';
CLF = CLF';
C_Ver = C_Ver';
C_Hor = C_Hor';
C_V = 10.^(C_Ver/20);
C_H = 10.^(C_Hor/20);
C_Mag = sqrt(C_V.^2 + C_H.^2);


%% OUPUT POWER OF THE ERS
%-------------------------
% Calculation of the radiated power
%-----------------------------------

% received voltage in V
V_V  = 10.^(VdB_Peak/20)*1e-6;
H1_V = 10.^(H1dB_Peak/20)*1e-6;
H2_V = 10.^(H2dB_Peak/20)*1e-6;

% Prad in watt
Zc = 50;
Prad_V_w  = (V_V.^2)/Zc;
Prad_H1_w = (H1_V.^2)/Zc;
Prad_H2_w = (H2_V.^2)/Zc;

% The power radiated by the ERS (using IEC 61000-4-21 E.2) in watt
Prad_ERS_V  = Prad_V_w.*A_eff./(CLF.*IL.*Loss_C.^2);
Prad_ERS_H1 = Prad_H1_w.*A_eff./(CLF.*IL.*Loss_C.^2);
Prad_ERS_H2 = Prad_H2_w.*A_eff./(CLF.*IL.*Loss_C.^2);


%%  EVALUATION OF GMAX
%---------------------
r = sqrt(H.^2+S^2);
r1 = sqrt((H-h).^2+S^2);
r2 = sqrt((H+h).^2+S^2)

% Horizontal polarisation
%-------------------------
for i=1:length(F)
    lambda = 3e8/F(i);
    Hmax_temp = abs((r./r1).*exp(-j*2*pi*r1/lambda) - (r./r2).*exp(-j*2*pi*r2/lambda));
    Hmax(i) = max(Hmax_temp);
    Hmax = Hmax';
end

% Vertical polarisation
%-----------------------
M = S.^2./r1.^2;
```

```
N = S.^2./r2.^2;
for i=1:length(F)
    lambda = 3e8/F(i);
    Vmax_temp = abs(M.*(r./r1).*exp(-j*2*pi*r1/lambda) + N.*(r./r2).*exp(-j*2*pi*r2/lambda));
    Vmax(i) = max(Vmax_temp);
    Vmax = Vmax';
end

%% OATS ELECTRIC FIELD EQUIVALENT AT 3m
%-----------------------------------------
% Directivity of the ERS
%-------------------------
D = 3.3113; % corresponds to a max gain of 5.2 dB
R = 3;

% OATS Electric field equivalent in uV/m
E_ERS_V  = (Vmax.*sqrt(D.*Prad_ERS_V*377./(4*pi*R.^2)))*1e6;
E_ERS_H1 = (Hmax.*sqrt(D.*Prad_ERS_H1*377./(4*pi*R.^2)))*1e6;
E_ERS_H2 = (Hmax.*sqrt(D.*Prad_ERS_H2*377./(4*pi*R.^2)))*1e6;
```